

**Flutter Suppression of a Flexible Flying-Wing UAV  
Using the Leading Edge Stagnation Point Sensor**

**A THESIS  
SUBMITTED TO THE FACULTY OF THE GRADUATE  
SCHOOL  
OF THE UNIVERSITY OF MINNESOTA  
BY**

**Adrià Serra Moral**

**IN PARTIAL FULFILLMENT OF THE REQUIREMENTS  
FOR THE DEGREE OF  
MASTER OF SCIENCE**

**Peter Seiler, Advisor**

**September, 2016**

© Adrià Serra Moral 2016  
ALL RIGHTS RESERVED

## Abstract

The increasing interest in making aircraft more fuel-efficient has led to lighter and inherently flexible aircraft. The performance benefits of lighter and more flexible structures can result in aeroservoelastic instabilities (flutter) that can cause catastrophic structural failure. Hence, active flutter suppression is a key technology to avoid flutter across the entire flight envelope while exploiting the performance benefits of flexible aircraft. In literature, accelerometers and rate-gyros that measure structural responses are commonly used for flutter suppression. Yet, a new paradigm that is known as "aerodynamic observable" seeks out for methods to sense the aerodynamic environment in real-time. The *Senflex*<sup>®</sup> hot-film sensor developed by *Tao Systems* has been shown to be effective at measuring the local lift coefficient ( $C_L$ ) in real-time. Consequently, it is important to understand the potential tradeoffs of using the lift coefficient as an available output for control synthesis. This thesis presents a framework for addressing the potential use of  $C_L$ -output feedback for suppressing the body-freedom flutter (BFF) mode of a flexible flying-wing drone. Hence, 2 controllers are designed: one controller uses the local vertical acceleration as the system output while the other uses the local  $C_L$ . Then, the performance and the robustness of both controllers are compared. To compare both outputs, first, the thesis presents a framework procedure to augment the flight-dynamics model so that it includes the local  $C_L$  as an output. In order to obtain similar designs and to ease the comparison, a "classic" single-input and single-output control approach is used. The performance of the controller is addressed by comparing the open-loop and the closed-loop damping ratios of the BFF mode. The robustness is address by comparing the classic gain and phase margins. Furthermore, a root-locus study is presented to select the most effective (at suppressing the BFF mode) choice of sensor location and the control effector pair. Initially, both controllers are integrated onto a flight-dynamics model that only considers the "bare-frame" of the flexible drone. Later, the model is augmented to include actuator dynamics, sensor dynamics, and a computational time delay. This augmentation is done on a buildup manner in order to understand how sensitive each controller is to the extra parasite dynamics that are present in real aircraft.

# Contents

List of Figures	iii
List of Tables	v
<b>1 Introduction</b>	<b>1</b>
<b>2 Aerodynamic Observable</b>	<b>5</b>
<b>3 Mini-MUTT: The Flying-Wing UAV</b>	<b>11</b>
3.1 Flight Dynamics Model . . . . .	13
3.2 Open-Loop Flutter Analysis . . . . .	17
<b>4 Active Flutter Suppression</b>	<b>20</b>
4.1 Control Effector and Sensor Location . . . . .	22
4.2 Closed-Loop Performance . . . . .	25
<b>5 Robustness Analysis</b>	<b>32</b>
5.1 Actuator Dynamics . . . . .	32
5.2 Sensor Dynamics . . . . .	36
5.3 Time Delays . . . . .	38
<b>6 Conclusion</b>	<b>43</b>
<b>Bibliography</b>	<b>45</b>

# List of Figures

1.1	Example of Unsuppressed Flutter and Catastrophic Structural Failure [36]	2
2.1	ASE Model Event Flowchart	6
2.2	Example of Critical Aerodynamic Flow Feature Indicators (CAFFIs)	7
2.3	LESP Location in the Conformally-Mapped Plane	8
2.4	Circuit of CVA Hot-Film Element	9
2.5	Wing Section Equipped with the <i>Senflex</i> <sup>®</sup> Hot-Film Sensor [31]	10
3.1	Mini-MUTT Flying-Wing Drone [26]	12
3.2	Mini-MUTT Vehicle Parts	12
3.3	Mini-MUTT Control Surfaces	12
3.4	Aeroelastic Vehicle Modeling Methodology	13
3.5	Mini-MUTT Rigid States, Control Inputs, and System Outputs	15
3.6	Mini-MUTT Mode Shapes of Interest	17
3.7	Mini-MUTT Lift-Curve Slope Distribution [26]	18
3.8	Airspeed Root Locus of Mini-MUTT Flight-Dynamics Model	19
3.9	Illustration of "Elastic Short-Period Mode" Eigenvector	19
3.10	Illustration of "1st Aeroelastic Mode" Eigenvector	19
4.1	Block Diagram of AFS Loop	21
4.2	Root Locus Comparison: Effect of Increasing y-Location of Accelerometer	22
4.3	Root Locus Comparison: Effect of Increasing y-Location of LESP Sensor	23
4.4	Root Locus Comparison: Accelerometer vs. LESP Sensor	25
4.5	Bode Diagram of Disturbance Sensitivity Beyond Flutter Speed	27
4.6	Root Locus Comparison of Controllers in Fig. 4.1 Including a Washout Filter	28
4.7	Bode Diagram of Disturbance Sensitivity Beyond Flutter Speed for Controller in Fig. 4.1 Including a Washout Filter	30
4.8	Time Response Comparison to a L3R3 ( $\delta_3$ ) Step Input	31
4.9	L1R1 ( $\delta_1$ ) Control Effort to the L3R3 ( $\delta_3$ ) Step Input in Fig. 4.8	31

5.1	Block Diagram of Controllers Including Flap Actuator Dynamics . . . . .	33
5.2	Root Locus Comparison of Controllers in Fig. 5.1 . . . . .	33
5.3	Bode Diagram of Disturbance Sensitivity Beyond Flutter Speed for Controllers in Fig. 5.1 . . . . .	35
5.4	Time Response Comparison to a L3R3 ( $\delta_3$ ) Step Input for the System in Fig. 5.1	35
5.5	Block Diagram of Controllers Including Both Actuator and Sensor Dynamics	36
5.6	Root Locus Comparison of Controllers in Fig. 5.5 . . . . .	37
5.7	Block Diagram of Controllers Including Actuator Dynamics, Sensor Dynamics, and Time-Delay . . . . .	38
5.8	Root Locus Comparison of Controllers in Fig. 5.7 with $\tau_{ms} = 13.2$ [ms] . . .	41

# List of Tables

4.1	Open-Loop Eigenvalues, Damping Ratios, and Natural Frequencies of the mini-MUTT Aircraft at 33.5 [m/s] . . . . .	21
4.2	Root Locus Summary: Effects of Sensor Placement and Actuator Pair on Closed-Loop Damping Ratios (Tailored to damp the BFF mode) . . . . .	24
4.3	Comparison of Open-Loop and Closed-Loop Damping Ratios for System in Fig. 4.1 with $\zeta_{\text{BFF}_{az}} = 0.6$ and $\zeta_{\text{BFF}_{CL}} = 0.64$ . . . . .	26
4.4	Comparison of Robustness Parameters for System in Fig. 4.1 with $\zeta_{\text{BFF}} = 0.0886$ (Both Controllers) . . . . .	26
4.5	Comparison of Open-Loop and Closed-Loop Damping Ratios for Controllers in Fig. 4.1 Including a Washout Filter with $\zeta_{\text{BFF}_{az}} = 0.6$ and $\zeta_{\text{BFF}_{CL}} = 0.64$ . . . . .	29
4.6	Comparison of Robustness Parameters for Controllers in Fig. 4.1 Including a Washout Filter with $\zeta_{\text{BFF}} = 0.20$ (Both Controllers) . . . . .	29
5.1	Comparison of Open-Loop and Closed-Loop Damping Ratios for Controllers in Fig. 5.1 with $\zeta_{\text{BFF}_{az}} = 0.6$ and $\zeta_{\text{BFF}_{CL}} = 0.63$ . . . . .	34
5.2	Comparison of Robustness Parameters for Controllers in Fig. 5.1 with $\zeta_{\text{BFF}} = 0.188$ (Both Controllers) . . . . .	34
5.3	Comparison of Open-Loop and Closed-Loop Damping Ratios for Controllers in Fig. 5.5 with $\zeta_{\text{BFF}_{az}} = 0.6$ and $\zeta_{\text{BFF}_{CL}} = 0.62$ . . . . .	37
5.4	Comparison of Robustness Parameters for Controllers in Fig. 5.5 with $\zeta_{\text{BFF}} = 0.164$ (Both Controllers) . . . . .	38
5.5	Time Delay and Corresponding Phase Results for Controllers in Fig. 5.7 with $K_{az} = 0.00183$ and $K_{CL} = 0.668$ . . . . .	39
5.6	Comparison of Open-Loop and Closed-Loop Damping Ratios for System in Fig. 5.7 . . . . .	40
5.7	Robustness Parameters of All the Augmented Systems Designed to Have the Same Closed-Loop Value of $\zeta_{\text{BFF}}$ . . . . .	42
5.8	Performance of All the Augmented Systems Designed to Have the Same Closed-Loop Value of $\zeta_{\text{ESP}}$ . . . . .	42

# Chapter 1

## Introduction

The main contributor to the total operating cost of an aircraft is fuel [10]. Hence, the aviation industry has set goals to make next generation aircraft more fuel-efficient. For instance, NASA is pursuing research to lower fuel consumption 60 percent by 2030-35 [4]. In [27], the author derives the expression for the rate of fuel burn of an aircraft in quasi-steady cruise, which can be expanded to match the form presented in Eq. 1.1.

$$\frac{dW}{dt} = -\frac{W}{(C_L/C_D)I_{sp}} \quad (1.1)$$

where  $W$  [lbs] is the aircraft's gross weight,  $C_L$  [unitless] is the total lift coefficient,  $C_D$  [unitless] is the total drag coefficient, and  $I_{sp}$   $\left[\frac{\text{lbs}}{\text{lbs/sec}}\right]$  is the engine specific impulse. Note that the engine's specific impulse is defined as the pounds of thrust produced per each pound of fuel consumed per second, so, it is another measure of the engine's efficiency. Eq. 1.1 shows that there are three ways to effectively reduce the rate of fuel burn: (1) increasing the engine's specific impulse; (2) reducing the aircraft's total weight; and (3) decreasing the total drag coefficient. Note that changes in the total lift coefficient are not considered, as the lift coefficient is fixed by the total weight. Not surprisingly, points (1) and (2) can be addressed by making engines more efficient and by using low-density composite materials for the structural design respectively. If we recall that the drag coefficient equation is,

$$C_D = \underbrace{C_{D_o}}_{\text{Profile Drag}} + \underbrace{\frac{C_L^2}{\pi A Re}}_{\text{Induced Drag}} \quad (1.2)$$

we see that the drag coefficient can be effectively reduced by decreasing the profile drag or by increasing the wing's aspect ratio. Since the profile drag is a function of the aircraft geometry [9], one way to reduce it would be to use airfoils with lower thickness or to shrink the fuselage diameter. The combination of everything has led to lighter, thinner, longer, and more slender wings, which has resulted in inherently flexible aircraft.

Traditionally, aircraft were assumed to be rigid, i.e. high-frequency structural dynamics and low-frequency rigid-body modes. Hence, aerospace engineers treated the study of aircraft stability and control in two different disciplines: flight mechanics and aeroelasticity. The frequency separation between "rigid-body" and "aeroelastic" modes allowed for claiming that the aeroelastic effects had a small influence on determining the aircraft flight mechanics, i.e. the aircraft maneuverability and loads. Hence, many flight-dynamics textbooks excluded aeroelastic effects when developing aircraft models and real-time simulations [3, 6, 28]. In practice, there were some attempts to include aircraft flexibility effects. For example, flexibility effects were included in the form of transfer functions on top of the rigid-body dynamics. These attempts were limited in scope and mainly captured changes in the overall aircraft stability [18]. Now, as the flexibility increases, structural modes decrease in frequency and they begin to impact the frequency range of "rigid-body" modes. Indeed, in Ref. 8 the author demonstrates that for very flexible aircraft the frequency separation between flight dynamic and aeroelastic modes can disappear. As both disciplines are now coupled, the study of aircraft stability and control needs to be treated as a unique aeroelastic discipline.

Aeroelasticity is the discipline that studies the interactions between aerodynamics, structural dynamics, and the vehicle motion. Flutter is arguably the most important subject in the study of aeroelasticity. Flutter occurs when aerodynamics and flexible deformations interact in an unstable manner, allowing the structure to effectively extract energy from the fluid stream. This unstable interaction can lead to a resonance-like behavior that can have catastrophic consequences (e.g., structural failure). An example of unsuppressed flutter that led to catastrophic structural failure is shown in Figure 1.1. The snapshots show the results of open-loop flutter during a flight test conducted at the University of Minnesota on August 25th, 2015, in which the mini MUTT aircraft (see Chapter 3) was pushed to slightly above its flutter speed of 30 m/s indicated airspeed. If looked carefully, both wing and fuselage torsion can be appreciated from the second snapshot of Figure 1.1 while wing bending can be appreciated from the third snapshot. This coupling between the aircraft's short-period mode with the combination of vehicle torsion and wing bending is known as body freedom flutter. Nonetheless, flutter is not a unique phenomenon as it can take different forms



Figure 1.1: Example of Unsuppressed Flutter and Catastrophic Structural Failure [36]

depending on the pair of interacting modes. For instance, there can be fuselage twisting and wing bending, coupled wing torsion and bending, or even control surface flutter. With the increasing use and authority of high-bandwidth automatic flight control systems,

modern aircraft can experience unstable interactions between the flight controller and the aeroelastic modes. This interaction can also lead to a resonance-like behavior that can result in the control surfaces fluttering. Subsequently, the field of aeroelasticity can be augmented to include the study of the flight control system interactions as well. The resulting discipline is typically denominated as aeroservoelasticity [43]. To ensure safety and aircraft certification, all forms of flutter must be avoided across the entire flight envelope.

Traditionally, aeroservoelastic instabilities were assessed passively during the design process by making changes to the vehicle configuration. Some of these changes included stiffening the structures or adding moving masses to change the vehicle inertia. Both changes resulted in added components, which increased the aircraft's total weight and fixed the flutter problem to the expense of overall performance (see Eq. 1.1). Therefore, flutter analysis involved many hours of wind-tunnel testing and the production of aeroelastically scaled models, adding to the design cost [35]. Furthermore, if the instabilities were to be observed through flight testing or during the certification process, the cost to change the vehicle design would be too high and impractical. Then, the aircraft commercialization would be placed in jeopardy. Thus, the aeroservoelastic research community was triggered to focus on flutter suppression methods using active controls, thereby fixing both problems at once. Although active flutter suppression (AFS) has been extensively researched since the mid-1960s, there has only been a few flight tests to demonstrate the technology in actual flight [13]. The recent development of NASA's re-configurable X-56 Multi-Utility Technology Testbed (MUTT) has allowed for a suitable platform for development, testing, and demonstration of AFS concepts [23]. Hand-in-hand with the control law is the choice of the proper input-output pair. One of the main challenges of AFS is the development of a required model that accurately captures the flutter dynamics. In Ref. 43, the authors demonstrate the importance of modeling unsteady aerodynamic effects to accurately characterize flutter. Modeling unsteady aerodynamics is very challenging and it is subject to significant uncertainty. As a result, a new paradigm known as "fly-by-feel" or "aerodynamic observable" seeks for methods to sense the aerodynamic environment in real-time as opposed to modeling it. Tao System's *Senflex*<sup>®</sup> hot-film sensor has shown that this paradigm is possible [15]. Consequently, it has allowed for considering a new interesting research field of AFS methods that use the sensed aerodynamic environment as load-output feedback.

This research introduces the active flutter suppression of a flexible drone using the local lift coefficient as the system output. To do so, first, a flight-dynamics model of a flexible flying-wing drone is augmented to include the local lift coefficient as a system output. Then, 2 similar controllers are designed: one controller uses the local acceleration ( $a_z(y)$ ) as the system output while the other uses the local lift coefficient ( $C_L(y)$ ). After, the performance and robustness of both controllers are compared. The goal of the comparison is to detect potential tradeoffs of controllers using the *Senflex*<sup>®</sup> hot-film sensor with respect to controllers using accelerometers. Again, the scope of this research is limited to addressing the potential tradeoffs through the comparison; therefore, this thesis does not consider the study of new and/or more effective control strategies. The following chapter contains a

background overview of the aerodynamic observable paradigm. Chapter 3 describes the methodology and process that was used to obtain a flight-dynamics model of the flying-wing drone, including the steps to augment the model so that it includes the local lift coefficient as a system output. Chapter 4 contains the closed-loop control synthesis when considering a perfect model, i.e. a model with perfect sensors, perfect actuators, and no time delays. Chapter 5 studies the effects of augmenting the model to include actuator dynamics, sensor dynamics, and a computational time delay on the total performance and robustness of each controller. The last chapter serves as a conclusion and provides suggestions for future work.

# Chapter 2

## Aerodynamic Observable

Modeling is an important part of control design. A good model for control design needs to accurately replicate the dynamics of interest of the real system while remaining simple, i.e., low-order. A typical ASE model that captures the coupled structural dynamics and aerodynamics is presented in [43] and has the following form:

$$\mathbf{A}\ddot{\mathbf{q}} + (\rho U_o \mathbf{B} + \mathbf{D})\dot{\mathbf{q}} + (\rho U_o^2 \mathbf{C} + \mathbf{E})\mathbf{q} = 0 \quad (2.1)$$

where  $\mathbf{A}$  is the structural inertia matrix,  $\mathbf{B}$  is the aerodynamic damping matrix,  $\mathbf{C}$  is the aerodynamic stiffness matrix,  $\mathbf{D}$  is the structural damping matrix,  $\mathbf{E}$  is the structural stiffness matrix, and  $\mathbf{q}$  is the vector of generalized coordinates of interest (e.g., angle-of-attack, pitch rate, etc). Also in [43], the authors show the importance of modeling unsteady aerodynamics in order to accurately predict flutter speeds and capture flutter effects. Consequently, matrices  $\mathbf{B}$  and  $\mathbf{C}$  are reduced frequency-dependent and need to be evaluated at the reduced frequency of interest. Modeling unsteady aerodynamics is challenging. Unsteady aerodynamic models are a function of both the aircraft kinematics (structural states) and the airflow wake. Therefore, unsteady aerodynamic models such as Theodorsen's lift coefficient model in [37], require the inclusion of the wake and the motion history through frequency-dependent lag states. This results in higher-dimension models that are usually more complex. In fact, this is one of the main challenges of ASE modeling. Lag states are typically inferred from the inertial states, resulting in higher propagated uncertainties. Consequently, the design of robust flutter suppression control laws is subject to more conservative margins of safety and is still a challenging active area of research. A new research direction seeks to sense the spatio-temporal aerodynamic environment in real-time as opposed to modeling it [15]. Sensing the aerodynamic environment in real-time, even in adverse conditions that are difficult to model such as separated flows (e.g., stall), is expected to reduce modeling uncertainty and make AFS methods more efficient. The block diagram of the events of an ASE vehicle in flight is included in Fig. 2.1. Disturbances or control surfaces inputs have a direct effect on the aerodynamic loading, which in turn changes the structural loading as well. Changes in structural loading can produce deformations of the vehicle structure and/or vibrations about the trimmed geometry. Inertial sensors (e.g., accelerometers) capture these structural

dynamics. As a result, inertial measurements lag the real physics of the aircraft model. Aerodynamic sensing in real-time would create a shortcut that would skip the structural dynamics in the dashed red box of Fig. 2.1. In other words, control laws using aerodynamic measurements would eliminate bandwidth-limiting inertial lag. Also, aerodynamic parameters used for modeling ASE vehicles are usually obtained using computational methods. Later, aerodynamic parameters are further updated using flight-data and system identification methods. Without the aerodynamic observable, aerodynamic loading and important aerodynamic states (e.g., angle of attack) need to be inferred from the inertial states and the vehicle kinematics [19]. This process usually results in higher propagated uncertainties. Hence, aerodynamic observable would also improve parameter identification techniques, resulting in aerodynamic parameters with smaller uncertainty bounds. Furthermore, Ref. 1 and Ref. 15 propose flutter suppression and aeroelastic control using an energy approach. This approach consists of tracking the aerodynamic work in real-time and ensuring that it remains strictly negative over the period of one harmonic oscillation. The aerodynamic work is a function of both the aerodynamic loading and the inertial response, both measurable in real-time. Hence, this method would not require the use of an ASE model, thereby, eliminating modeling uncertainty.

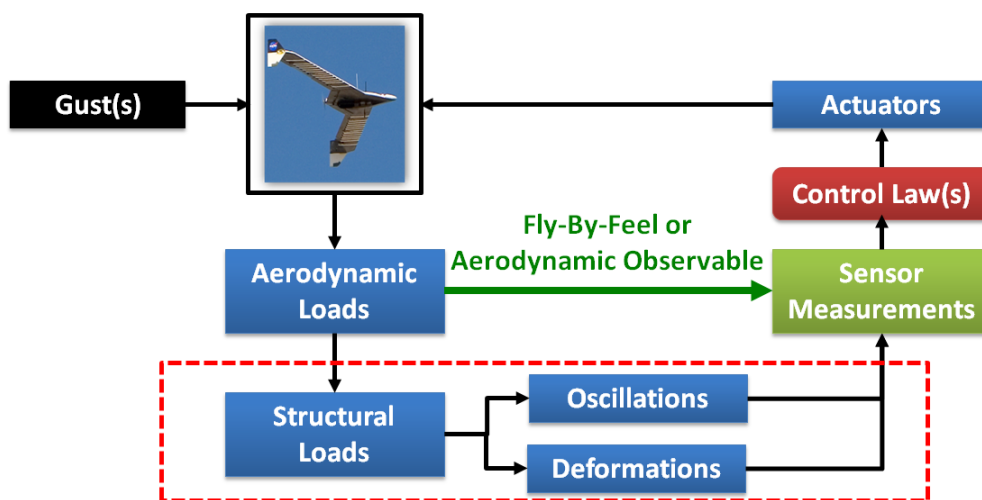


Figure 2.1: ASE Model Event Flowchart

The aerodynamic environment, or the circulation around a wing, can be captured by tracking critical aerodynamic flow feature indicators (CAFFIs). Examples of such indicators might include the leading-edge stagnation point (LESP), the flow separation point (FSP), the flow reattachment point, the laminar-to-turbulent transition point, etc. The LESP is where the flow attaches to the wing, causing the local velocity of the flow to be zero, while the FSP is where the flow detaches from the wing. An example of both the LESP and the FSP in a two-dimensional airfoil in flight is illustrated in Fig. 2.2. The effects of the aerodynamic topology (i.e., the location and movement of CAFFIs over an

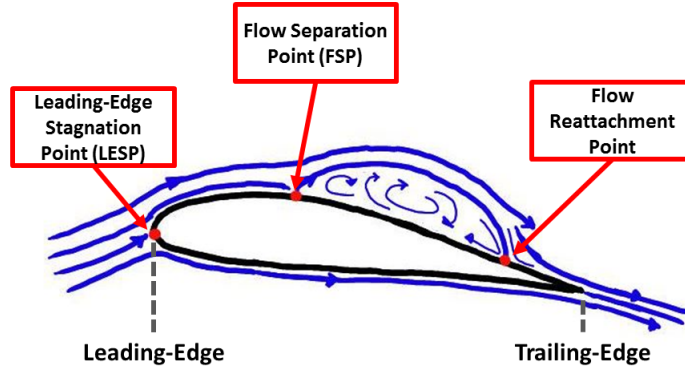


Figure 2.2: Example of Critical Aerodynamic Flow Feature Indicators (CAFFIs)

airfoil) on the total circulation for subsonic potential flows are described by L.C. Woods in [42]. For fully-attached flows, the circulation around the airfoil can be determined by the imposed Kutta-Joukowski condition, which enforces the rear stagnation point to be located at the sharp trailing-edge [9]. Then, the location of the LESP is dependent on the total circulation around the airfoil. For fully-attached flows, the location of the LESP moves downstream (towards the trailing-edge) as the total circulation increases and vice versa. Ref.31 shows that, under the assumption of fully-attached flows, the location of the LESP is a monotonic function of the angle-of-attack (AoA). In fact, the LESP location is shown to be just a scaled-multiple of the AoA. The location of the FSP is dependent on the pressure gradient across the airfoil. When the airflow is unable to negotiate an adverse pressure gradient, the flow separates, creating an FSP and causing the trailing-edge stagnation point to move upstream (as shown in Fig. 2.2). This results in a loss of the total circulation, which in turn causes the LESP to move upstream. Consequently, the effects of both fully-attached and separated flows can be effectively captured by just tracking the LESP location. Even though there are many aerodynamic books that include this high-level analysis, references in the literature that include an analytic relationship between the LESP location and circulation are scarce. In 2015, an unsteady aerodynamic model was developed in [31] based on the LESP location and control surface deflection. The derivation follows an approach similar to Theodorsen's theory for oscillating airfoils. In this model, the LESP location is defined as the angle ( $\delta$ ) between the free-stream velocity and the point of zero local velocity in a conformally-mapped plane using the Joukowski transformation. Then, this angle  $\delta$  can be mapped back to the physical plane as a linear distance ( $x_\delta$ ) from the wing leading-edge. The LESP location in both the conformally-mapped and the physical planes is depicted in Fig. 2.3. The main findings included in [31] are: (1) both the lift coefficient and the AoA are monotonic functions of  $\delta$ , which depend only on the airfoil geometry; (2) the location of the flexural (or elastic) axis does not appear in the final form of the equations, which is an important (and useful) finding as the location of the elastic axis is usually difficult to estimate for complex wing designs; (3) the relationship between unsteady lift coefficient and  $\delta$  is observed to be memoryless, i.e., the final form of the equation does not depend on lag states or the motion history.

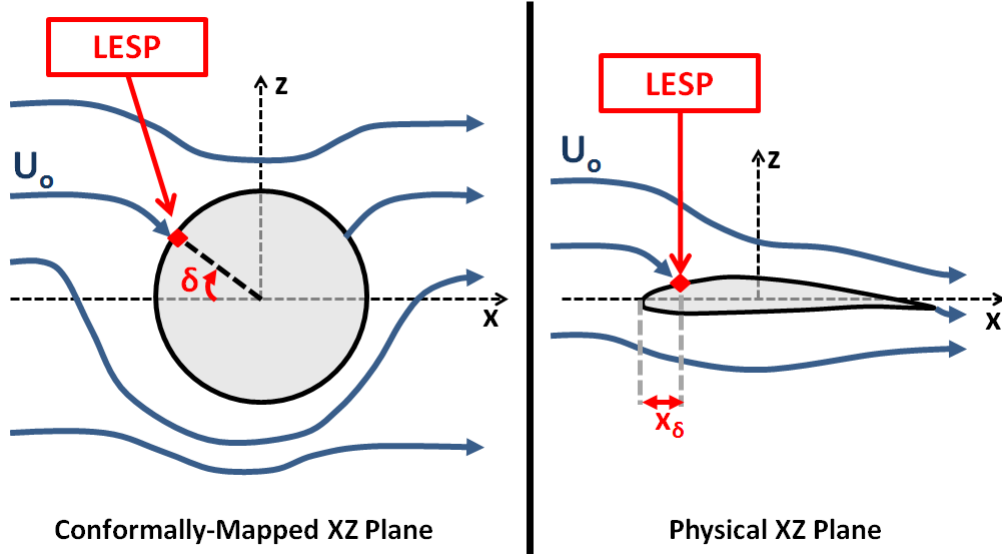


Figure 2.3: LESP Location in the Conformally-Mapped Plane

Traditionally, there have been different methods and sensors used to predict the flow state and/or measure the topology of CAFFIs. Examples of such include the use of pressure sensors, pressure transducers, pressure sensitive paint, accelerometers, strain gauges, hot-film sensors, etc. Unfortunately, most of these sensors have major disadvantages that make them unsuitable for measuring CAFFIs in real-time [16]. Pressure sensors can be used to predict aerodynamic loading by direct integration of the pressure distribution over the wing. However, they require significant set-up times and calibration as pressure strongly depends on both temperature and/or density conditions, both which change often in flight. Accelerometers and strain gauges can be used to predict aerodynamic loads from the structural and inertial responses. This is a major problem as aerodynamics lead structural responses; therefore, the inferred aerodynamic measurements are always lagging the true CAFFI dynamics. Furthermore, the aerodynamic measurements inferred from accelerometers and strain gauges are only as accurate as the models used to derive them which, as mentioned earlier, are subject to high uncertainties. Hot-film sensors can be used in thermal anemometry to obtain CAFFI topology by measuring the amount of heat dissipated from the heated sensor to the airstream. This method effectively measures the shear stress (i.e., the fluid viscosity), which by definition is tangential to the flow. Also, the sensor does not involve mechanical or moving parts, thereby obtaining measurements with relatively high frequency and minimal lag. Moreover, hot-film sensors can be easily embedded with composite laminates without using adhesives, polymer films, or major structural modifications, allowing for a simple non-intrusive design that can be used even in harsh environments (see Fig. 2.5). However, not all forms of hot-film thermal anemometry are suitable for real-time aerodynamic sensing. Conventional constant current anemometry is limited by the large time-constants that are required. Constant temperature anemometry is complex to set-up as it can create a potential sensor failure.

If the temperature decreases, the sensor experiences an increase in current to keep the temperature constant, which could lead to overcurrent failure if the temperature decreased enough. Moreover, changes in atmospheric temperature affect the amount of heat that is transferred from the heated sensor to the fluid, adding biases to the sensor readings. Nonetheless, these limitations can be effectively mitigated by using an array of hot-film sensors with constant voltage anemometry and a data acquisition and processing technique called phase-reversal signatures (as patented by Siva M. Mangalam and Tao Systems in [17]).

The diagram of Tao System’s constant voltage anemometer circuit is published in [34], which can be slightly modified to include the hot-film sensor element as depicted in Fig. 2.4. From the circuit, the voltage across the hot-film element  $V_{HF}$  [Volts] can be represented as:

$$V_{HF} = \frac{R_1}{R_2} V_1 \quad (2.2)$$

where  $R_1$  [Ohms] and  $R_2$  [Ohms] are fixed resistors, and  $V_1$  [Volts] is a variable voltage source. Hence, the value of  $V_1$  can be chosen such that the hot-film element is heated to any desired

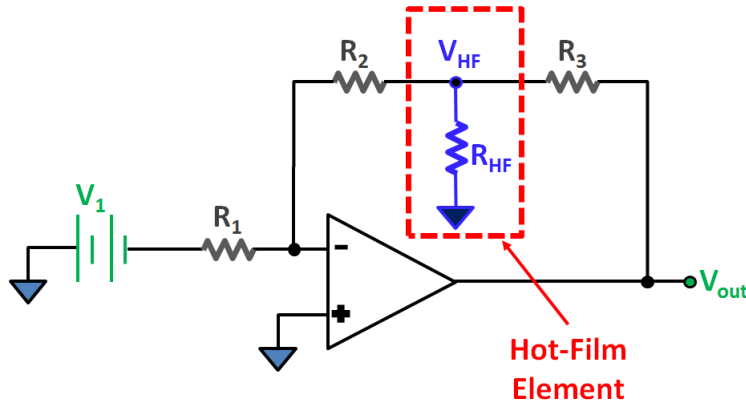


Figure 2.4: Circuit of CVA Hot-Film Element

temperature, due to Joule Heating. The desired temperature is chosen to be greater than the atmospheric stagnation temperature to ensure convective heat transfer from the sensor to the flow. The output voltage  $V_{out}$  [Volts] from the circuit in Fig. 2.4 can be represented as:

$$V_{out} = \left( 1 + \frac{R_3}{R_1} + \frac{R_3}{R_{HF}} \right) V_{HF} \quad (2.3)$$

where  $R_3$  [Ohms] is another fixed resistor,  $R_{HF}$  [Ohms] is the resistance value of the hot-film sensor element, and  $V_{HF}$  [Volts] is the voltage across the hot-film element as in Eq. 2.2. The hot-film sensor element is made out of nickel, so, its resistance varies with the element temperature. Nickel’s resistance increases as the temperature increases [12]. Also, as the local convective heat transfer depends on the local airflow velocity [2], the sensor element’s temperature depends on the local airspeed across it. As a result, the sensor element’s

resistance ( $R_{HF}$ ) depends directly on the magnitude of the airspeed across it.  $R_{HF}$  decreases as the flow velocity increases. Consequently, the output voltage in Eq. 2.3 increases as the flow velocity increases. Recall that the LESP location corresponds to the point where the local airflow velocity is zero. Hence, the flow accelerates as it moves away from the LESP point. Consequently, the voltage output of the hot-film element that is located at the LESP point is at a local minimum when compared to the readings of the hot-film elements on either side of it. Also, signals from sensors located on the same side of the bifurcation are in-phase while signals from sensors located across the flow bifurcation experience a phase-reversal. All in all, the location and movement of CAFFI points can be determined by tracking the location of minimum voltage signals and/or phase reversal between adjacent sensors. Notice that this method does not depend on the actual magnitudes of the voltage readings but it depends on the comparison between the readings of adjacent sensors. This is very suitable for aerodynamic sensing in real-time as the method shows to be immune to changes in the flow condition and shows to have high signal-to-noise ratio. For more detailed information, refer to [17]. This technique is implemented on the *Senflex*<sup>®</sup> multi-element surface hot-film sensors developed by *Tao of Systems, Inc.*

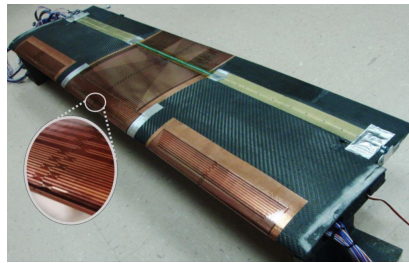


Figure 2.5: Wing Section Equipped with the *Senflex*<sup>®</sup> Hot-Film Sensor [31]

For simplicity, the *Senflex*<sup>®</sup> sensor will be referred as the "LESP sensor" moving forward in this thesis. Texas A&M University, in collaboration with Tao Systems, has embedded the LESP sensor to a wing section (see Fig. 2.5) and conducted wind tunnel experiments to demonstrate the success on measuring the wing's lift coefficient in real-time [31, 30]. In Ref. 31, the author presents the wind tunnel results for both static and dynamic tests. The static test consists of an angle-of-attack sweep from  $-8$  to  $+8$  degrees for three control surface deflections:  $-5$ ,  $0$ , and  $+5$  degrees. The dynamic test consists of a frequency sweep in the trailing-edge control surface in which the wing section is only allowed to pitch. In both cases, the lift coefficients inferred by measuring the LESP location is shown to be an almost perfect match to the lift coefficients obtained by both the thin-airfoil theory and the wind-tunnel load sensor. Hence, the LESP sensor is shown to work for sensing the local lift coefficient in real-time. The next chapter includes the main steps on developing a flight-dynamics model of the flexible flying-wing drone that includes local lift coefficient as a system output.

# Chapter 3

## Mini-MUTT: The Flying-Wing UAV

As mentioned in [13], there have been only a handful of flight tests to prove AFS methods in actual flight. If the controller test was to be unsuccessful, both the test-pilot engineer's life and the vehicle would be in critical danger. In fact, as compiled in Ref. 40, the history of flutter is full of losses in both lives and vehicles. Thereby, the aviation industry inclined towards avoiding flutter in the entire flight envelope. The use of unmanned aerial systems (UAS), also known as drones, can be a solution to that problem. The market for drones has been growing drastically over the recent years [21]. UAS are versatile and have relatively low initial costs, as well as operation expenses. Hence, they serve as a suitable platform for research and development of safety-critical technologies. Since there is no pilot onboard a drone, the major risks of AFS testing may be accepted. The drone of interest in this thesis is called "mini-MUTT" and it is depicted in Fig. 3.1 and Fig. 3.2. The mini-MUTT was designed and constructed at the University of Minnesota (UMN). Its geometry resembles Lockheed Martin's Body-Freedom Flutter vehicle, designed to test AFS-methods in flight. In fact, the mini-MUTT was built after Lockheed Martin donated their last BFF vehicle to the UMN to help expand the aeroservoelastic research program. The mini-MUTT is a remote-piloted flying wing that is designed to flutter at low speeds. It has a wingspan of 10 ft. (3 m) and a total gross weight of roughly 14.7 lbs. (6.7 Kg). As shown in Fig. 3.2, the vehicle is composed of three major parts: the center-body and the pair of detachable wings. The center-body is assumed to be rigid and contains all the major electronics. Attached to the back of the center-body is an electric motor with a pusher propeller. The wings are swept-back for longitudinal stability, contain winglets on the wingtips for lateral-directional stability, and are assumed to be flexible. For control, the wing trailing-edge consists of eight control surfaces, four on each side (see Fig. 3.3). The first control surface pair (L1 and R1) is known as the body flaps. The next pair (L2 and R2) is known as the first mid-board flaps. The following pair (L3 and R3) is known as the second mid-board flaps. Lastly, the last pair (L4 and R4) is known as the outboard flaps. The next section describes the methodology that was followed to obtain a flight-dynamics model of the mini-MUTT.

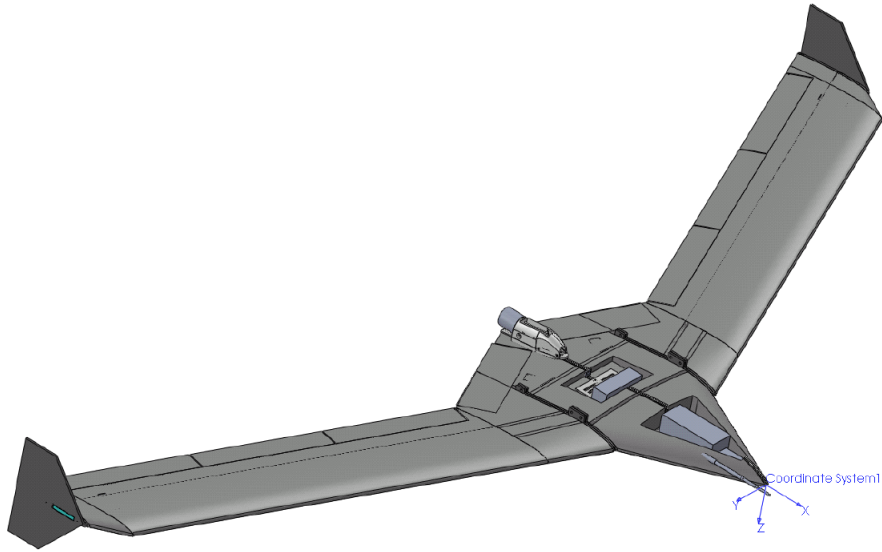


Figure 3.1: Mini-MUTT Flying-Wing Drone [26]

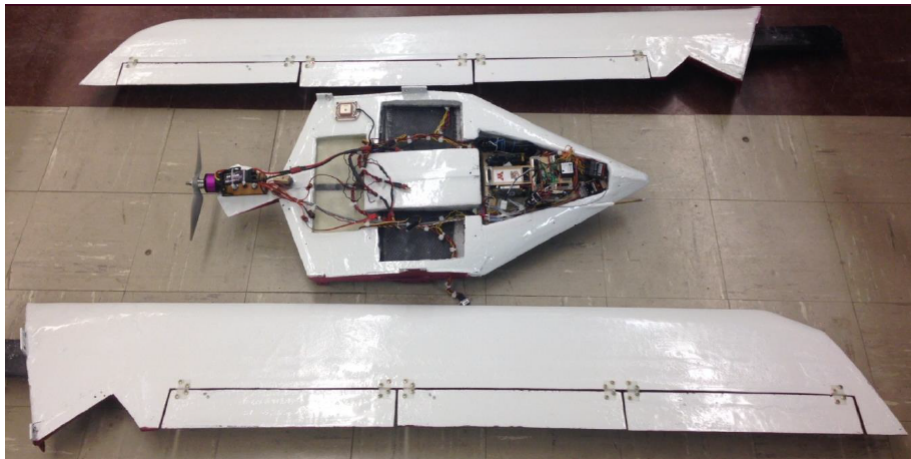


Figure 3.2: Mini-MUTT Vehicle Parts

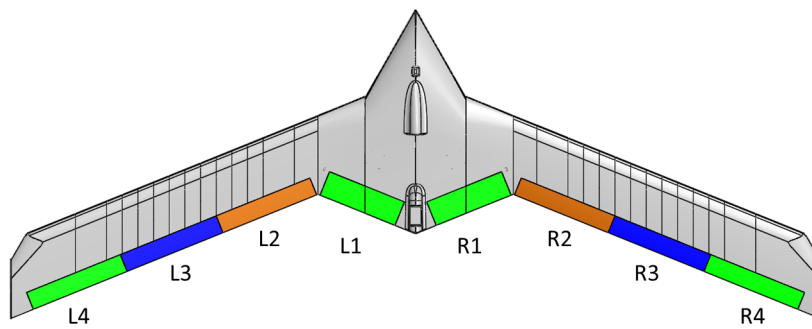


Figure 3.3: Mini-MUTT Control Surfaces

### 3.1 Flight Dynamics Model

As mentioned in the Introduction, obtaining a model that mimics the dynamics of interest is an important part of control design. A suitable model for AFS must capture the structural dynamics, the “rigid-body” dynamics, and the interactions between the two. In literature, it is possible to distinguish two major methodologies to model aeroelastic vehicles. In Ref. 26, the author refers to these approaches as the “flutter” models and the “flight-dynamics” models. The “flutter” models start by deriving an accurate structural model with coupled aerodynamics, which is then augmented to include some rigid-body degrees of freedom (DoFs). On the other hand, the “flight-dynamics” model starts by modeling the vehicle as a rigid body, which is then augmented to include flexible DoFs. The main difference between the two methodologies is in the coordinate frames that are used to derive the equations of motion. “Flutter” models are typically defined in the inertial reference frame while “flight-dynamics” models use a body-referenced frame. While both methodologies have advantages of their own, the model used for this thesis followed a “flight-dynamics” approach as both onboard sensors and aerodynamic responses are defined in a body-fixed coordinate frame, making the model compatible with control design.

The methodology followed to derive the aeroservoelastic model of the mini-MUTT is presented in [3] and depicted in the Fig. 3.4. The figure shows the main “blocks” and pieces

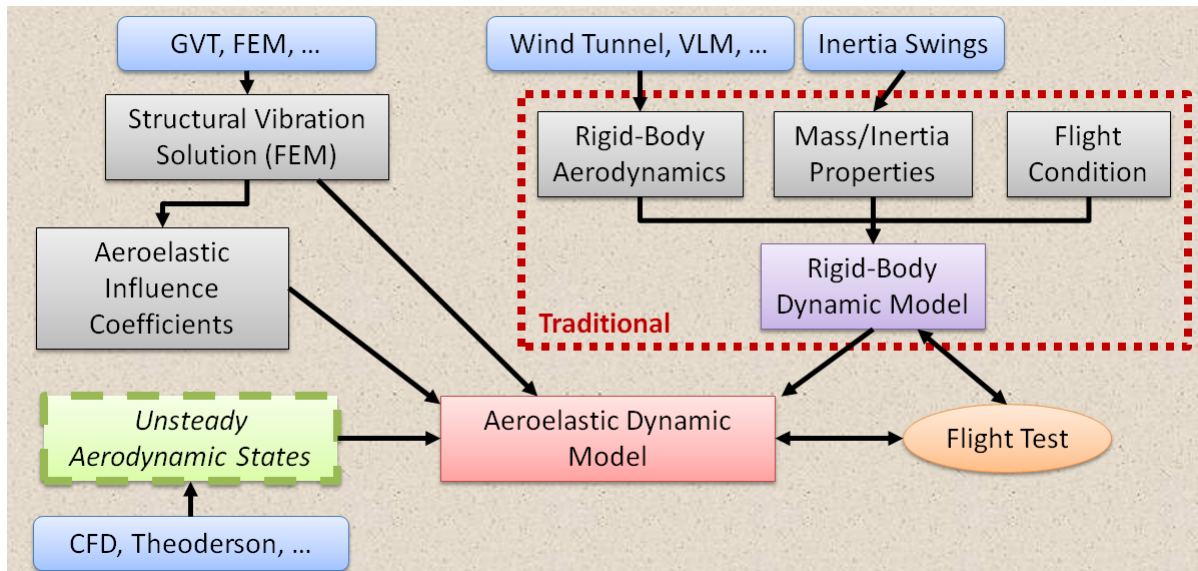


Figure 3.4: Aeroelastic Vehicle Modeling Methodology

that are required to obtain the dynamic model. In this approach, the body-referenced coordinate frame that was used to derive the equations of motion was based on a mean-axes description [38]. The origin of the mean-axes is attached to the instantaneous center of mass of the vehicle, which, due to elastic deformations, is not constant with time. The orientation of the mean-axes is defined such that both the relative translational and angular

momentum of the entire aircraft, due to elastic deformations, are zero at every instant of time. Hence, the mean-axes are said to move or “float” in phase with the motion and deformation of the vehicle [43].

First, the aeroelastic drone is assumed to be rigid, and the rigid-body equations of motion are derived following any of the methods that are extensively found in the literature [24, 27, 6, 3]. These methods are still consistent with the mean-axes description as, if the vehicle is assumed to be rigid, both the location of the center of mass and the moments of inertia are fixed with time. In this case, the origin of the mean-axes is fixed with respect to the aircraft and its orientation can be chosen arbitrarily. Then, the mean-axis description is observed to match either the body-fixed or stability axes used to derive stability and control derivatives. The aerodynamic stability and control derivatives of the mini-MUTT were obtained using a vortex-lattice method [11]. Second, the rigid-body model is augmented to include the structural flexibility effects. Here, the drone vibration solution is obtained from a finite beam-element model [26], which is updated and optimized using the results obtained from ground vibration tests [7]. Then, the vibration solution is used to derive the aeroelastic coefficients using quasi-steady or unsteady strip-theoretic techniques [47]. This method is analogous to deriving the stability and control derivatives of a rigid aircraft. Hence, the main advantage of this approach is that it results in a parametrized aeroservoelastic model that is consistent with flight mechanics and flight-control theory. Furthermore, another advantage of this method is that the parametrized model is obtained early in the design cycle. Later, the model can be further updated using flight-test data and parameter identification methods [20].

The current model considers only longitudinal dynamics for straight and level flight under small elastic deformations from the trimmed geometry. The final form of the model follows the standard linearized state-space formulation [41], included in Eqn. 3.1-3.2.

$$\dot{X} = AX + Bu \tag{3.1}$$

$$Y_{sensor} = CX + Du \tag{3.2}$$

The first four states correspond to the three rigid-body DoFs and are identical to those of a rigid aircraft, namely the forward surge velocity  $u_{rig}$  [ft/s], the angle of attack  $\alpha_{rig}$  [rad], the pitch angle  $\theta_{rig}$  [rad], and the pitch rate  $q_{rig}$  [rad/s] (see Fig. 3.5). These states describe the motion of the body-fixed frame or mean axes. The last  $2n$  states correspond to the  $n$  elastic DoFs, described by the generalized displacements  $\eta$  [rad] and the generalized velocities  $\dot{\eta}$  [rad/s]. Since the mini-MUTT is designed to exhibit two symmetric flutter conditions in the longitudinal axis, only the first three symmetric modes are included in the model, i.e., the first two symmetric bending modes and the first symmetric torsion mode. The resulting state-space dynamic system of Eq. 3.1 takes the form given in Eq. 3.3. Note that the system

is composed of rigid-body (subscript R) and elastic (subscript E) subsystems.

$$\dot{X} = \begin{bmatrix} X_u & X_\alpha & -g & X_q & 0 & 0 & \cdots & 0 & 0 \\ Z_u/V & Z_\alpha/V & 0 & 1 + Z_q/V & Z_{\eta_1}/V & Z_{\dot{\eta}_1}/V & \cdots & Z_{\eta_3}/V & Z_{\dot{\eta}_3}/V \\ 0 & 0 & 0 & 1 & 0 & 0 & \cdots & 0 & 0 \\ M_u & M_\alpha & 0 & M_q & M_{\eta_1} & M_{\dot{\eta}_1} & \cdots & M_{\eta_3} & M_{\dot{\eta}_3} \\ 0 & 0 & 0 & 0 & 0 & 1 & \cdots & 0 & 0 \\ 0 & \Xi_{1\alpha} & 0 & \Xi_{1q} & \Xi_{1\eta_1} - \omega_1^2 & \Xi_{1\dot{\eta}_1} - 2\omega_1\zeta_1 & \cdots & \Xi_{1\eta_3} & \Xi_{1\dot{\eta}_3} \\ \vdots & \vdots & \vdots & \vdots & \vdots & \vdots & \cdots & \vdots & \vdots \\ 0 & 0 & 0 & 0 & 0 & 0 & \cdots & 0 & 1 \\ 0 & \Xi_{3\alpha} & 0 & \Xi_{3q} & \Xi_{3\eta_1} & \Xi_{3\dot{\eta}_1} & \cdots & \Xi_{3\eta_3} - \omega_3^2 & \Xi_{3\dot{\eta}_3} - 2\omega_3\zeta_3 \end{bmatrix} X + \begin{bmatrix} X_{\delta_1} & \cdots & X_{\delta_4} \\ Z_{\delta_1}/V & \cdots & Z_{\delta_4}/V \\ 0 & \cdots & 0 \\ M_{\delta_1} & \cdots & M_{\delta_4} \\ 0 & \cdots & 0 \\ \Xi_{1\delta_1} & \cdots & \Xi_{1\delta_4} \\ \vdots & \cdots & \vdots \\ 0 & \cdots & 0 \\ \Xi_{3\delta_1} & \cdots & \Xi_{3\delta_4} \end{bmatrix} u$$

$$\dot{X} = \begin{bmatrix} A_{RR} & A_{RE} \\ A_{ER} & A_{EE} \end{bmatrix} X + \begin{bmatrix} B_R \\ B_E \end{bmatrix} u \quad (3.3)$$

Here, the entries  $X$ ,  $Z$ ,  $M$ , of the rigid subsystem are dimensional aerodynamic, stability, or control derivatives;  $Z_\eta$ ,  $M_\eta$ , and  $\Xi_\eta$  are aeroelastic derivatives;  $\omega_k$  and  $\zeta_k$  for  $k = 1, 2, 3$  are the eigenfrequencies and damping ratios (respectively) of the  $k^{\text{th}}$  structural mode; and  $g$  is the gravitational acceleration constant. It is important to emphasize that the dimensional derivatives of the dynamic model depend directly on the dynamic pressure, i.e., depend on the flight condition defined by the altitude and airspeed (see Fig. 3.4). The system's state vector is  $X = [u_{rig} \ \alpha_{rig} \ \theta_{rig} \ q_{rig} \ \eta_1 \ \dot{\eta}_1 \ \eta_2 \ \dot{\eta}_2 \ \eta_3 \ \dot{\eta}_3]^T$  and the current system considers four control inputs  $u = [\delta_1 \ \delta_2 \ \delta_3 \ \delta_4]^T$ ; here, the inputs  $\delta_i$  consist of the symmetric deflections of the  $i^{\text{th}}$  pair of flaps (see Fig. 3.5). Note that neither unsteady aerodynamic lag states nor actuator dynamics are considered for the linearized model included in Eq. 3.3.

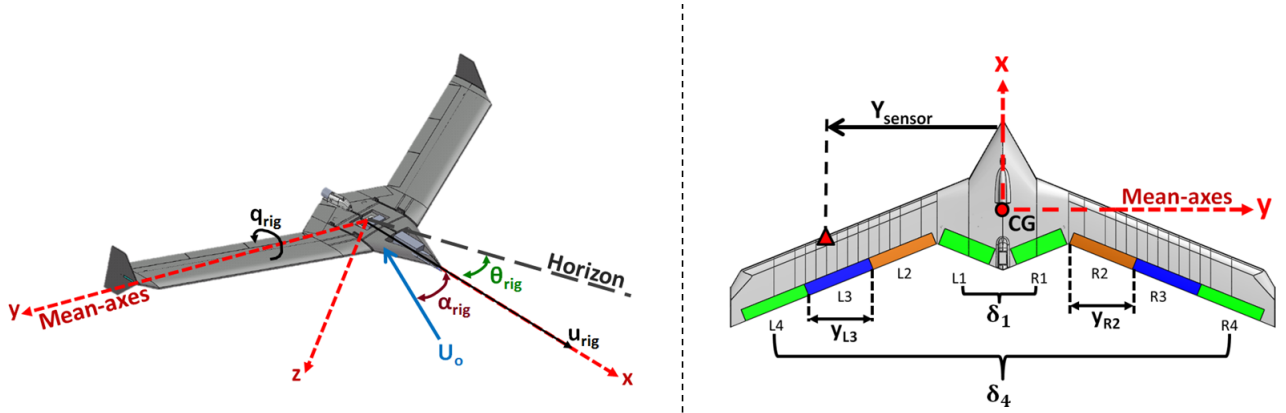


Figure 3.5: Mini-MUTT Rigid States, Control Inputs, and System Outputs

In accordance with the dynamic model, the sensor-output model is also derived following the general state-space formulation (Eq. 3.2). As argued earlier in the introduction, the research seeks to gain an understanding of flutter suppression using the LESP sensor. Later, the performance of the controller using the LESP sensor is compared to the performance of a benchmark design that uses an accelerometer. Also, as important as the choice

of sensor-actuator pair, is the placement of the sensor itself. Here, placing the sensor anywhere along the wingspan is assumed to be possible. Hence, the two sensor-outputs that need to be modeled are the local lift coefficient  $C_L$  and the local vertical acceleration  $a_z$  at any point along the wingspan, i.e.,  $Y_{sensor} = [C_L(y) \ a_z(y)]^T$ . To follow the general state-space formulation, both  $C_L$  and  $a_z$  must be modeled as linear functions of the system states  $X$  and the control inputs  $u$ . In Ref. 24, the author derives a general relationship for both  $a_z(x, y, z)$  and  $\alpha(x, y, z)$  as functions of the rigid-body states and the elastic generalized displacements/velocities. Both relationships can be adapted to match the form in the equations here:

$$a_z(y) = \underbrace{U_o \dot{\alpha}_{rig} - U_o q_{rig} + \Delta x_{sensor} \dot{q}_{rig}}_{\text{rigid contribution}} + \underbrace{\dot{\omega}_E(y)}_{\text{elastic contribution}} \quad (3.4)$$

$$\alpha(y) = \underbrace{\alpha_{rig} - \frac{\Delta x_{sensor} q_{rig}}{U_o}}_{\text{rigid contribution}} + \underbrace{\left( \theta_E(y) + \frac{\omega_E(y)}{U_o} \right)}_{\text{elastic contribution}} \quad (3.5)$$

where,

$$\theta_E(y) = \sum_{i=1}^3 \nu'_{Z_i}(y) \eta_i(y) \quad \omega_E(y) = \sum_{i=1}^3 \nu_{Z_i}(y) \dot{\eta}_i(y)$$

Here,  $U_o$  [ft/s] is the pre-defined free-stream velocity and  $\Delta x_{sensor}$  [ft] is the distance from the aircraft instantaneous center of gravity to the sensor in the x-axis. Note that all the parameters in both equations have been previously defined except for  $\nu_{Z_i}(y)$  and  $\nu'_{Z_i}(y)$ . These parameters depend on the mode shapes of the vehicle, which are available from the beam-element model. The first three symmetric mode shapes are depicted in Fig. 3.6. Note that  $Z$  is defined positive down and the wing-twist is defined positive leading-edge up (see Fig. 3.5). In Fig. 3.6, it can be seen that  $\nu_{Z_i}(y)$  [ft] is defined as the value of the plunge (z-axis) displacement of the  $i^{\text{th}}$  mode shape at the location of interest. Similarly,  $\nu'_{Z_i}(y)$  [rad] is defined as the value of the torsional displacement of the  $i^{\text{th}}$  mode shape at the location of interest. Lastly, assuming fully-attached flow, the local lift coefficient can be computed as a linear function of the local AoA, the local generalized displacements/velocities, and the local control surface deflections:

$$C_L(y) = C_{L_\alpha}(y) \alpha(y) + C_{L_q} q_{rig} + \sum_{i=1}^3 C_{L_{\eta_i}}(y) \eta_i + \sum_{i=1}^3 C_{L_{\dot{\eta}_i}}(y) \dot{\eta}_i + \sum_{j=1}^4 C_{L_{\delta_j}}(y) \delta_j \quad (3.6)$$

Here,  $C_{L_{\delta_j}}(y)$  [1/rad] is defined to be the 2-D control surface effectiveness, as determined by strip theory [9], if the y-location is within the range of the control surface  $y_{Lj}$  or  $y_{Rj}$  (see Fig. 3.5). Otherwise, it is assumed to be zero:

$$C_{L_{\delta_j}}(y) = \begin{cases} c_{l_{\delta_j}} & \text{if } y \in y_{Lj} \quad \text{or} \quad y \in y_{Rj} \\ 0 & \text{otherwise} \end{cases} \quad \text{for } j = \{1, 2, 3, 4\} \quad (3.7)$$

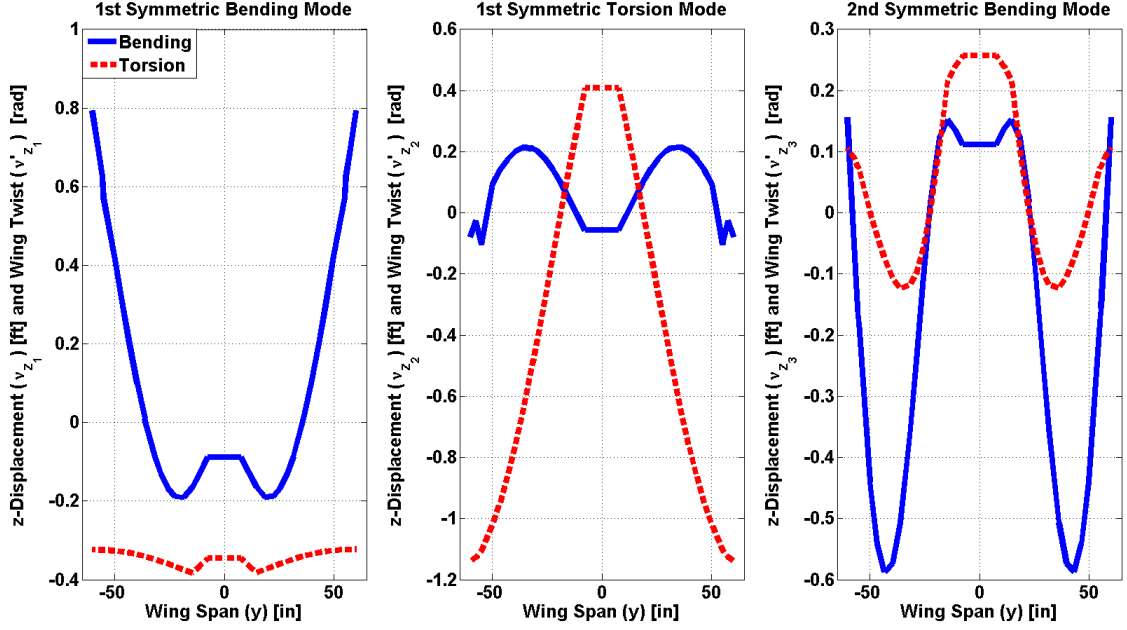


Figure 3.6: Mini-MUTT Mode Shapes of Interest

Analogous to the aerodynamic and stability derivatives,  $C_{L_{\eta_i}}(y)$  and  $C_{L_{\dot{\eta}_i}}(y)$  represent the changes in lift due to elastic deformations. Such coefficients are also defined in [24] as included in Eq. 3.8 and Eq. 3.9. Note that, in order to evaluate the integrals, the algebraic expressions of  $\nu_{Z_i}(y)$  and  $\nu'_{Z_i}(y)$  are obtained by fitting a polynomial to the mode shapes in Fig. 3.6.

$$C_{L_{\eta_i}}(y) = \frac{2}{S_w} \int_0^{\frac{b_w}{2}} C_{L_\alpha}(y) \nu'_{Z_i}(y) c_w(y) dy \quad (3.8)$$

$$C_{L_{\dot{\eta}_i}}(y) = \frac{2}{S_w U_o} \int_0^{\frac{b_w}{2}} C_{L_\alpha}(y) \nu_{Z_i}(y) c_w(y) dy \quad (3.9)$$

In Eq. 3.8-3.9,  $S_w$  [ft.<sup>2</sup>] is the total area of the wing,  $b_w$  [ft.] is the total wingspan, and  $c_w(y)$  [ft.] is the local chord length of an infinitesimal wingspan element. Finally,  $C_{L_\alpha}(y)$  [1/rad] is the value of the lift-curve slope, as determined from the vehicle vortex-lattice method [26], at the y-location of interest (see Fig. 3.7). The next section uses this linearized dynamic model to study the presence and characteristics of flutter.

## 3.2 Open-Loop Flutter Analysis

The study of flutter is performed considering the eigenvalues and eigenvectors of the aeroelastic dynamic model in Eq. 3.3. The top half of the airspeed root-locus showing the system's eigenvalue locations for three airspeeds (26, 30, and 33.5 m/s) is depicted in

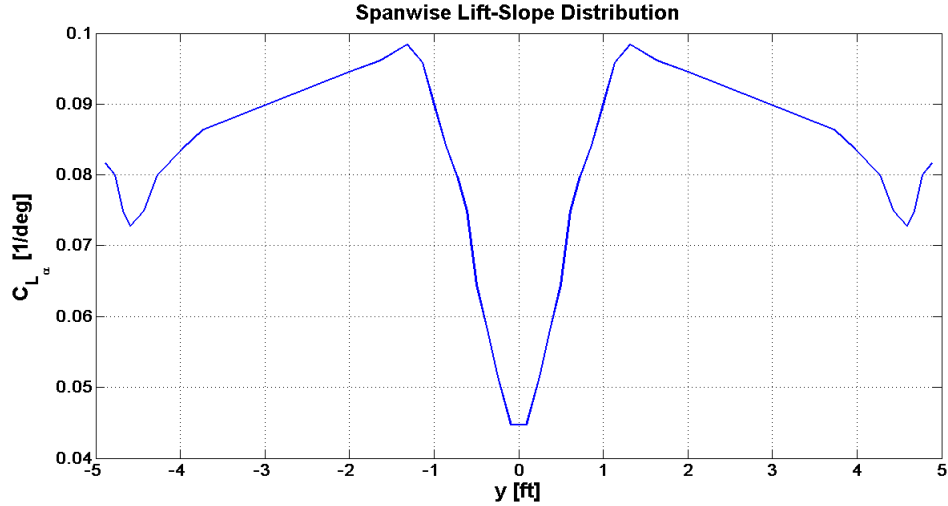


Figure 3.7: Mini-MUTT Lift-Curve Slope Distribution [26]

Fig. 3.8. In Fig. 3.8, notice how the branch identified as “1st aeroelastic mode” moves further to the right-half plane as the value of the airspeed increases. Eventually, this branch crosses the imaginary axis, proving the presence of flutter at a flight velocity slightly higher than 30 m/s. The mode branches are identified based on the most dominant states involved, which can be determined by observing the eigenvectors of each mode. For instance, the eigenvectors of the mode branch labeled as “elastic short period” at 30 m/s airspeed are shown in Fig. 3.9. Indeed, this mode is dominated by the rigid pitch rate with virtually non-dependence on the surge velocity, which is very similar to the short period mode of a rigid aircraft [24]. Yet, unlike the conventional short period, the eigenvectors show also a strong co-dependency with the elastic deformation rate. The eigenvectors of the “1st aeroelastic mode” at a flight velocity of 30 m/s are included in Fig. 3.10. The main contributor to this mode is the first structural vibration rate or the first symmetric bending rate. However, unlike a pure vibration mode, the second largest contributor to the “1st aeroelastic mode” is the rigid pitch rate. These two examples show that, as argued in the introduction, the aeroelastic drone does not have pure rigid-body and elastic modes, but it has a coupled product of the two. This “1st Aeroelastic” flutter condition that exhibits coupled symmetric bending and rigid-body short period is known as the body-freedom flutter condition. Also, note that both the flutter velocity and the flutter characteristics match the observations obtained from the open-loop flutter flight test performed by the University of Minnesota on August 25, 2015 (see Fig. 1.1).

The next chapter uses the linearized state-space model to design a controller that effectively suppresses the body-freedom flutter in closed-loop.

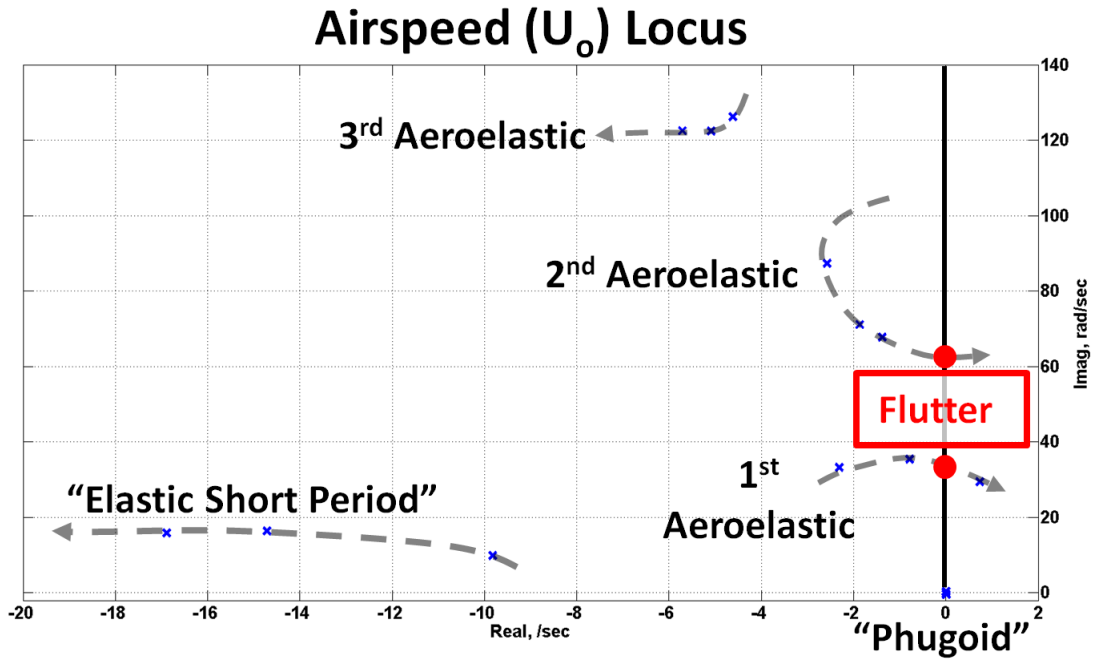


Figure 3.8: Airspeed Root Locus of Mini-MUTT Flight-Dynamics Model

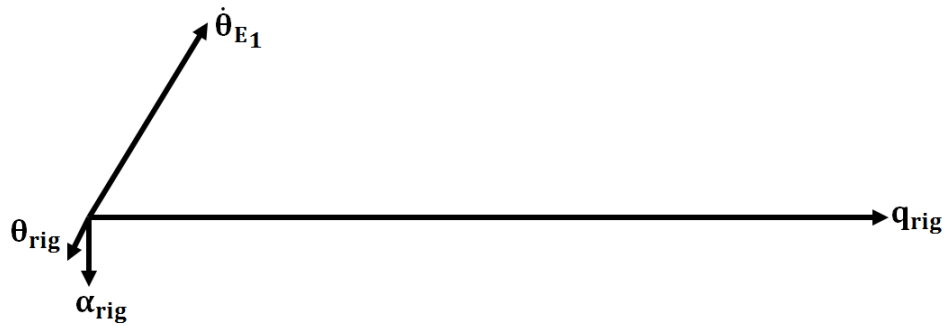


Figure 3.9: Illustration of "Elastic Short-Period Mode" Eigenvector

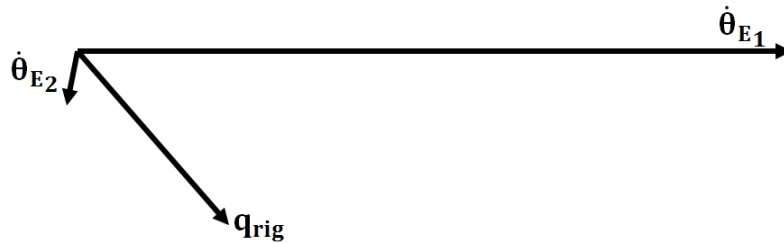


Figure 3.10: Illustration of "1st Aeroelastic Mode" Eigenvector

# Chapter 4

## Active Flutter Suppression

Since the focus of the aeroservoelastic community moved to AFS methods, there have been a large number of theoretical studies presented in literature. These studies consider both "classical" single-input and single-output (SISO) control approaches and more "modern" multivariable synthesis methods. Examples of SISO methods include the so-called collocated feedback (e.g., [22, 39]) and Identically Located Acceleration and Force (ILAF) (e.g., [44, 45, 25]). SISO methods are more easily designed using a root-locus analysis and do not require precise knowledge of the vehicle mode shapes. This offers favorable robustness properties as mode shapes are difficult to predict accurately. Yet, both collocated feedback and ILAF methods require the actuator and sensor pair to be placed at exactly the same location. This geometrical constraint may not be strictly satisfied in all aircraft. Examples of multivariable synthesis methods include LQG controllers (e.g., [14, 23]), LQR controllers (e.g., [46, 5]), and  $\mathcal{H}_\infty$  controllers (e.g., [36, 48]). These methods offer great robustness properties, which are desired in highly uncertain ASE systems. Yet, these methods often yield higher-order and more complex controllers. As noted in Ref. 25, these methods lack the transparency about the "cause-and-effect relationships between components in the control laws and the physics of the aircraft". Also, note that all the literature examples listed above used accelerometers as the available sensors. Examples of AFS methods that use aerodynamic observable methods include the  $C_L$ -tracker controllers in [32, 33]. The use of the LESP sensor in this "aerodynamic observable" paradigm is a relatively recent concept that is currently under investigation.

In this thesis, the controller method was chosen to be a SISO, ILAF-like approach. As mentioned, the main goal of this research is to understand the use of  $C_L$ -output for AFS through the comparison to a benchmark design that uses an accelerometer. Hence, a "classic" SISO method offers for a simpler controller architecture that is more transparent and easier to compare. Also, recall that the sensors were assumed to be placeable anywhere along the wingspan (see Chapter 3), allowing for the ILAF-like study. As a result, the control architecture of both controllers was chosen to be that of a simple proportional controller, as depicted in Fig. 4.1.

Table 4.1: Open-Loop Eigenvalues, Damping Ratios, and Natural Frequencies of the mini-MUTT Aircraft at 33.5 [m/s]

Eigenvalue	Damping Ratio ( $\zeta$ )	Natural Frequency ( $\omega_n$ [rad/s])	Mode Branch
$0.00378 \pm 0.348i$	-0.00109	0.348	Phugoid
$-16.9 \pm 15.9i$	0.729	23.2	Elastic Short Period
$0.735 \pm 29.5i$	-0.0249	29.5	BFF
$-1.38 \pm 67.8i$	0.0204	67.8	2 <sup>nd</sup> Aeroelastic Mode
$-5.71 \pm 122i$	0.0466	123	3 <sup>rd</sup> Aeroelastic Mode

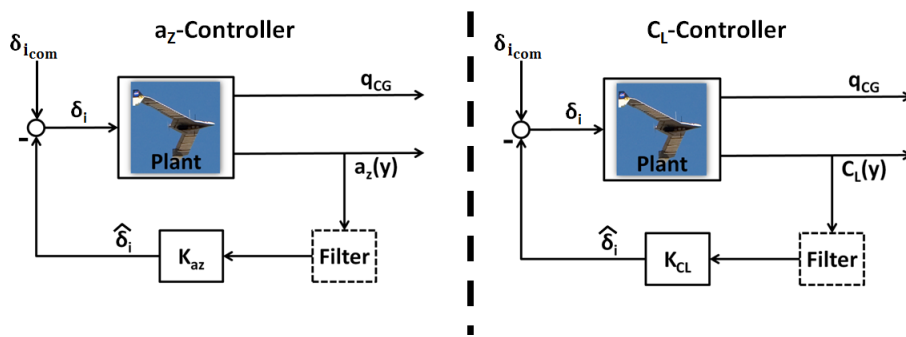


Figure 4.1: Block Diagram of AFS Loop

In Fig. 4.1,  $\hat{\delta}_i$  [rad] represents the symmetric deflection of one of the four available control input flaps as commanded by the flight controller. Similarly,  $\delta_{i,com}$  [rad] represents the symmetric deflection of one of the four available control input flaps as commanded by the pilot. Note that the same control input is used in both controllers. Also, both the accelerometer (measuring  $a_z(y)$ ) and the LESP sensor (measuring  $C_L(y)$ ) are placed in the same exact  $y$ -location along the wingspan. The output  $q_{CG}$  represents the elastic pitch rate as measured at the aircraft's center of gravity. The common pitch rate output of both controllers is used to allow for a more direct comparison. The dotted filter block indicates that a filter may or may not be added to the loop. If a filter is added, it is added to both controllers to allow for a similar comparison. The control input gains  $K_{az}$  and  $K_{CL}$  are chosen such that the same amount of damping on the BFF flutter mode is obtained. Hence, the magnitudes of the gains may not be the same. Then, the two controllers are compared in terms of their resulting performance and robustness. The performance is measured by comparing the percentage increase in damping of the remaining two aeroelastic modes. The robustness is measured using the classic gain margin (GM) and phase margin (PM). The aircraft model that is used for control design is linearized at 33.5 [m/s]. The eigenvalues, damping ratios, and natural frequencies of the open-loop system at such airspeed are included in Table 4.1. The next section includes the root-locus methodology used to compare the different input-output combinations and select the most suitable control effector and sensor location pair.

## 4.1 Control Effector and Sensor Location

The choice of control effector and sensor location pair is arguably an important part of control design. A different choice of the input-output pair may yield significantly different results on the closed-loop performance. In this thesis, the effects of different sensor placements and control actuator choices are studied qualitatively and through logic rather than using mathematical algorithms. The effects are studied by comparing the root locus of the control loops in Fig. 4.1. In this model, three sensor locations are considered: 20, 40, and 57.5 inches from the center of gravity. For simplicity, only the body flaps ( $\delta_1$ ) and the outboard flaps ( $\delta_4$ ) are considered for control design. The reason for that is to give full authority of the mid-board flaps ( $\delta_2$  and  $\delta_3$ ) to the pilot. Then, a total of six root locus are considered and compared for each sensor, resulting in twelve root locus overall. In Fig. 4.2, the control input is set to be the body flap ( $\delta_1$ ) and the effects of moving the accelerometer further along the wingspan are compared. Here, the airspeed is 33.5 [m/s], slightly beyond the flutter speed at which the BFF mode becomes unstable.

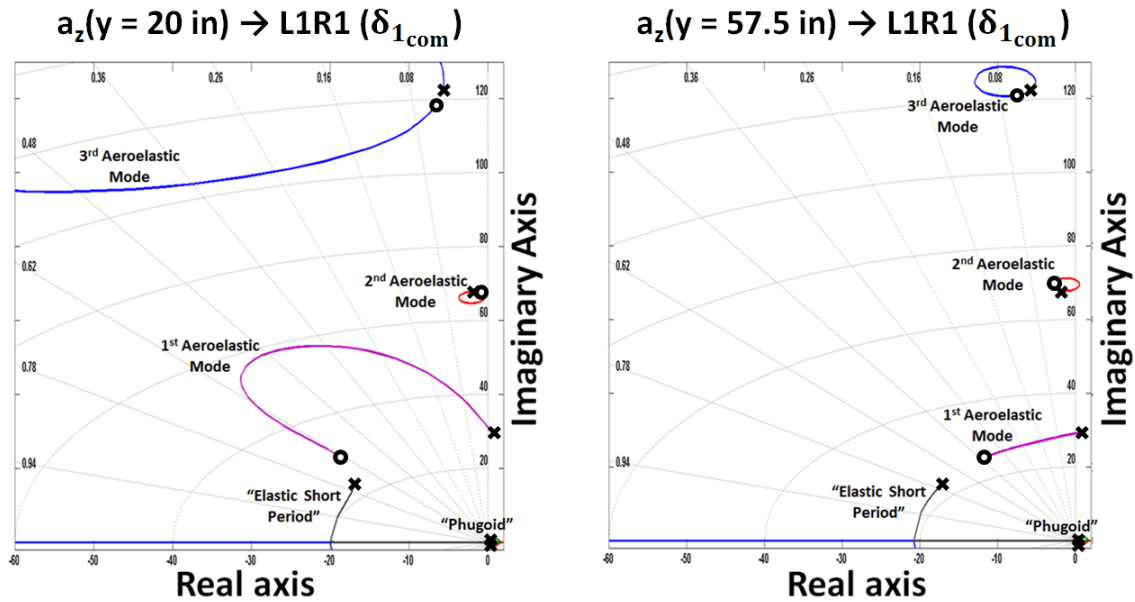


Figure 4.2: Root Locus Comparison: Effect of Increasing y-Location of Accelerometer

Note that placing the accelerometer at 20 inches allows for greater damping of the first and third aeroelastic modes than placing the accelerometer at 57.5 inches. It is important to mention that true ILAF is not possible in this system. A deflection of the flaps creates a distributed load and moment about the control surface area of the wing, as opposed to a point force or torque. Hence, both sensor locations can potentially increase damping of all aerolastic modes. Yet, placing the sensor closer to the actuator yields better results, since the sensor is closer (or within) the area where the distributed aerodynamic load is most observable. Similar results are observed in Fig. 4.3, in which the LESP sensor is used in place of the accelerometer.

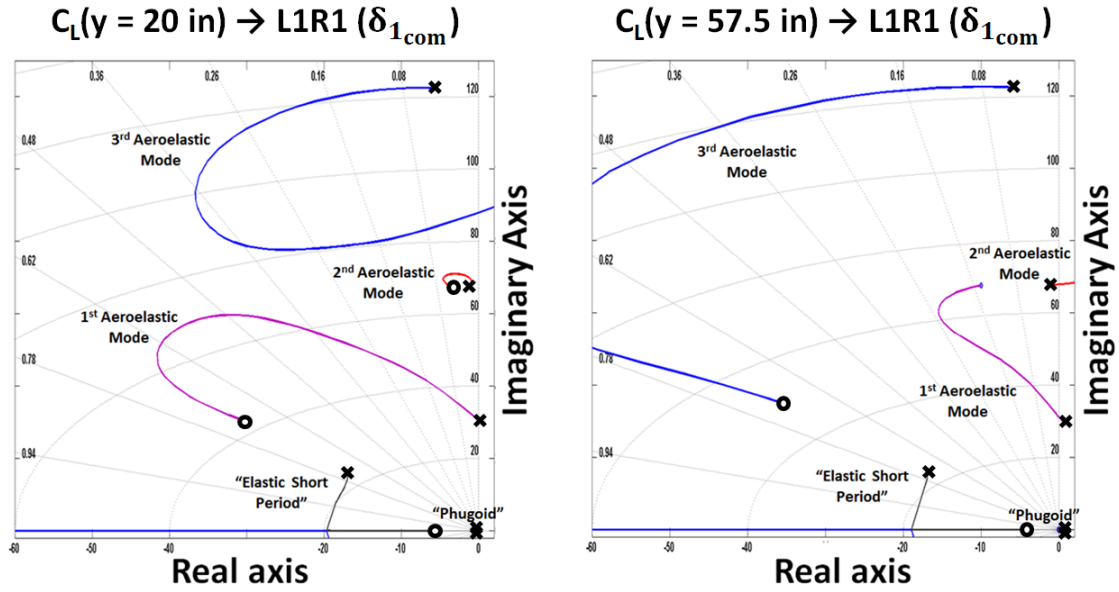


Figure 4.3: Root Locus Comparison: Effect of Increasing  $y$ -Location of LESP Sensor

For convenience, the main findings of all twelve root locus plots are summarized in Table 4.2. The values in Table 4.2 represent the maximum closed-loop damping ratio that can be achieved using each sensor, sensor location, and actuator pair combination. The value of the open-loop damping ratio at 33.5 [m/s] is displayed in parenthesis at each mode branch row. The maximum closed-loop damping ratio of the first aeroelastic mode, or BFF mode, is defined as the value of damping that can be achieved before one of the other two aeroelastic modes becomes unstable or the "elastic short period" (ESP) mode becomes over-damped. Then, the maximum percentage damping of both the second and third aeroelastic modes correspond to the values that are obtained as a consequence of damping the BFF mode. This is the reason why the closed-loop damping of either the second or the third aeroelastic modes may be worsened.

Table 4.2: Root Locus Summary: Effects of Sensor Placement and Actuator Pair on Closed-Loop Damping Ratios (Tailored to damp the BFF mode)

	y-location [in]	Sensor → Actuator Pair			
		$a_z(y) \rightarrow \delta_1$	$C_l(y) \rightarrow \delta_1$	$a_z(y) \rightarrow \delta_4$	$C_l(y) \rightarrow \delta_4$
		Closed-Loop $\zeta$	Closed-Loop $\zeta$	Closed-Loop $\zeta$	Closed-Loop $\zeta$
<b>BFF Mode</b> (Open Loop $\zeta_{\text{BFF}} = -0.0249$ )	20	<u>0.30</u>	<u>0.474</u>	0.0902	0.111
	40	0.066	0.281	0.10	0.12
	57.5	0.034	0.22	<u>0.12</u>	<u>0.16</u>
<b>2<sup>nd</sup> ASE mode</b> (Open Loop $\zeta_{\text{AE2}} = 0.0204$ )	20	<u>0.0294</u>	<u>0.0256</u>	0.011	0.022
	40	0.0286	0.005	0.014	0.024
	57.5	0.0145	0.003	<u>0.021</u>	<u>0.026</u>
<b>3<sup>rd</sup> ASE mode</b> (Open Loop $\zeta_{\text{AE3}} = 0.0466$ )	20	<u>0.11</u>	<u>0.232</u>	0.04	0.061
	40	0.02	0.106	0.036	0.060
	57.5	0.01	0.06	0.040	<u>0.063</u>

In Table 4.2, the underlined values represent the y-locations that offer the greatest percentage damping increase for each sensor choice and control input pair. Referring back to the ILAF-like system discussion, note how the percentage damping tends to decrease as the sensor is placed further from the actuator. Note that the third aeroelastic mode and the outboard flap input does not seem to follow the trend. In fact, any sensor location is observed to have a similar effect on the third mode damping. Looking at the mode shapes of the third mode in Fig. 3.6, it can be noticed that the outboard flaps are located close to two nodes. Hence, this control input is not very effective at damping the third aeroelastic mode and does not follow the ILAF theory that requires the input-output pair to be located away from a structural node. Moreover, the poor performance of both controllers at damping the second aeroelastic mode can also be deduced by looking at the mode shapes in Fig. 3.6. The main contributor to the second aeroelastic mode is the wing's torsion, which is not very observable by measuring linear acceleration. The chosen control strategy was tailored to damp the BFF mode. All in all, note how the designs that achieve the greatest damping of the BFF mode, and the most similar to one another, involve the sensors to be placed at 20 inches and the use of the body flaps. Hence, this sensor placement and actuator effector pair is chosen for control synthesis, i.e. the loop of Fig. 4.1 is closed with  $y = 20$  inches and  $i = 1$ . If the filter block is not included, the root locus of the resulting controller loops are included in Fig. 4.4. In the next section, the root locus in Fig. 4.4 are used to select the gains, and the performances of both controllers are compared.

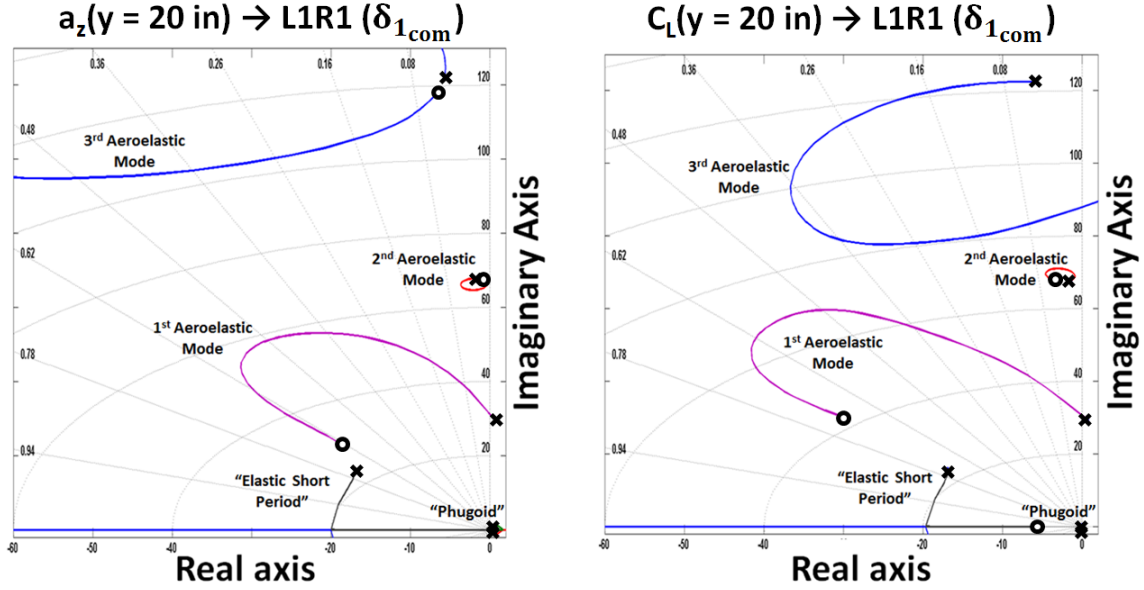


Figure 4.4: Root Locus Comparison: Accelerometer vs. LESP Sensor

## 4.2 Closed-Loop Performance

As mentioned in the previous section, the values of the controller gains are chosen such that the damping of the BFF mode is the same in both controllers. In addition, the values of the closed-loop elastic short period damping ( $\zeta_{ESP}$ ) should not vary significantly from the open-loop value. Hence,  $\zeta_{ESP}$  was ensured to be within the range in Eq. 4.1, allowing a percentage difference of about 18% from the optimal value of 0.71 that has traditionally been observed to offer balance between disturbance rejection and controllability [29].

$$0.6 \leq \zeta_{ESP} \leq 0.85 \quad (4.1)$$

Then, the performance of both controllers at damping the rest of the aeroelastic modes and the values of the classical gain and phase margins are compared. Again, the controllers in this thesis are design such that the following requirements are satisfied:

1. The damping ratio of the elastic short period is within the threshold in Eq. 4.1.
2. The closed-loop damping ratio of the BFF mode is the same for both controllers.
3. None of the remaining mode branches becomes unstable in closed-loop.

First, the filter block (see Fig. 4.1) is not considered, i.e. the filter block is defined as unity. The value of damping of the BFF mode ( $\zeta_{BFF}$ ) that can be achieved by both controllers

under these conditions is  $\zeta_{\text{BFF}} = 0.0886$ . This damping value is limited by  $\zeta_{\text{ESP}}$  of the  $a_z$ -Controller reaching the upper bound in Eq. 4.1. At the same ESP damping ratio value, the  $C_L$ -Controller could reach a BFF mode damping of  $\zeta_{\text{BFF}} = 0.140$ , which is a 58% higher than the value of the  $a_z$ -Controller. The open-loop and the resulting closed-loop damping ratios of all the aeroelastic mode branches are included in Table 4.3. The  $a_z$ -Controller is shown to result in a greater second aeroelastic mode damping without significantly modifying the third aeroelastic mode while the  $C_L$ -Controller is shown to result in the opposite. The classic robustness parameters (GM, PM, and the gain-crossover frequency) of both controllers are compared in Table 4.4.

Table 4.3: Comparison of Open-Loop and Closed-Loop Damping Ratios for System in Fig. 4.1 with  $\zeta_{\text{BFF}_{a_z}} = 0.6$  and  $\zeta_{\text{BFF}_{C_L}} = 0.64$

Controller	BFF Mode			2 <sup>nd</sup> Aeroelastic Mode			3 <sup>rd</sup> Aeroelastic Mode		
	Open-Loop $\zeta_{\text{BFF}}$	Closed-Loop $\zeta_{\text{BFF}}$	%- Increase	Open-Loop $\zeta_{\text{AE}_2}$	Closed-Loop $\zeta_{\text{AE}_2}$	%- Increase	Open-Loop $\zeta_{\text{AE}_3}$	Closed-Loop $\zeta_{\text{AE}_3}$	%- Increase
1 ( $a_z$ )	-0.0249	0.0886	455	0.0204	<u>0.0322</u>	<u>58</u>	0.0466	0.0455	-2.3
2 ( $C_L$ )					0.0173	-15		<u>0.0855</u>	<u>84</u>

Table 4.4: Comparison of Robustness Parameters for System in Fig. 4.1 with  $\zeta_{\text{BFF}} = 0.0886$  (Both Controllers)

Controller	$K_p$ -Gain	Gain Margin (dB)		Phase Margin (deg.)		Gain-Crossover Frequency (rad/s)
1 ( $a_z$ )	0.00172	-12	<u>4.3</u>	-131	11	40
2 ( $C_L$ )	0.449	-16	<u>31</u>	-139	<u>30</u>	38

In Table 4.4, the  $C_L$ -Controller is shown to have higher gain and phase margins than the  $a_z$ -Controller. The underlined values, or shadowed cells, in both Table 4.3 and Table 4.4 represent the controller values that are considered to have a better performance. Given these definitions, the  $C_L$ -Controller with the LESP sensor is observed to be more suitable for suppressing the BFF mode. In addition, the bode diagram of the *disturbance sensitivity* transfer function is included in Fig. 4.5. The *disturbance sensitivity* transfer function is defined from the input  $\delta_{1_{\text{com}}}$  to the common pitch rate output  $q_{\text{CG}}$  (see Fig. 4.1). More specifically, if the aircraft block in Fig. 4.1 is defined as a transfer function  $G(s)$ , the *disturbance sensitivity* transfer function is defined as:

$$\frac{q_{\text{CG}}}{\delta_{1_{\text{com}}}} = G(s)S(s) \quad (4.2)$$

In Eq. 4.2,  $S(s)$  represents the *input sensitivity* transfer function, which in the SISO system can be written as:

$$S(s) = (1 + K_p G(s))^{-1} \quad (4.3)$$

where  $K_p$  represents the controller gain.

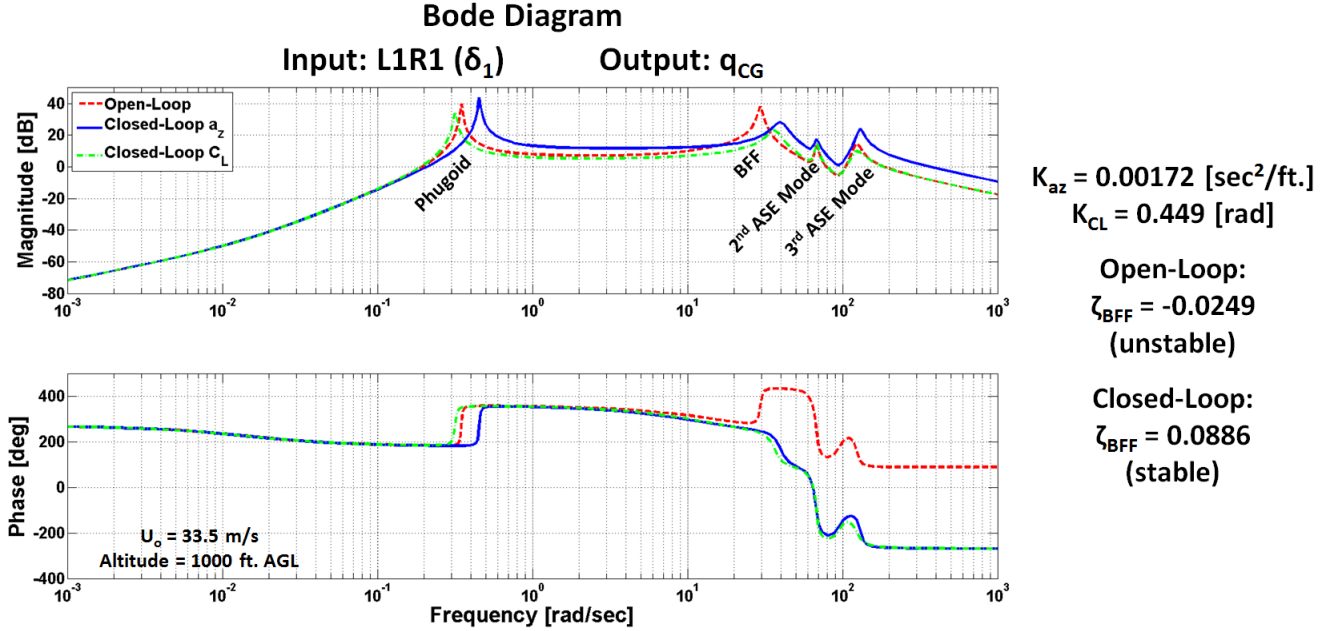


Figure 4.5: Bode Diagram of Disturbance Sensitivity Beyond Flutter Speed

In Fig. 4.5, the effects of the controllers on the "rigid-body" modes are more apparent. The closed-loop phugoid mode of both controllers is observed to change in frequency and slightly in damping as well, which is not desirable to maintain the handling-qualities of the aircraft unchanged. Other than that, the BFF resonant peak is shown to be reduced in magnitude, i.e. more damped.

In order to prevent the controller from altering the phugoid "rigid-body" dynamics, a washout filter is added to the controllers in Fig. 4.1. The washout filter is designed to have a cutoff frequency of 27 [rad/s], which is in between the ESP and the BFF modes. Thus, decreasing the controller action on the lower-frequency "rigid-body" dynamics. The form of the washout filter is included in Eq.4.4.

$$H_{FWO}(s) = \frac{s}{s + 27} \quad (4.4)$$

For completeness, the root locus of the two controllers that include the washout filter are included in Fig. 4.6.

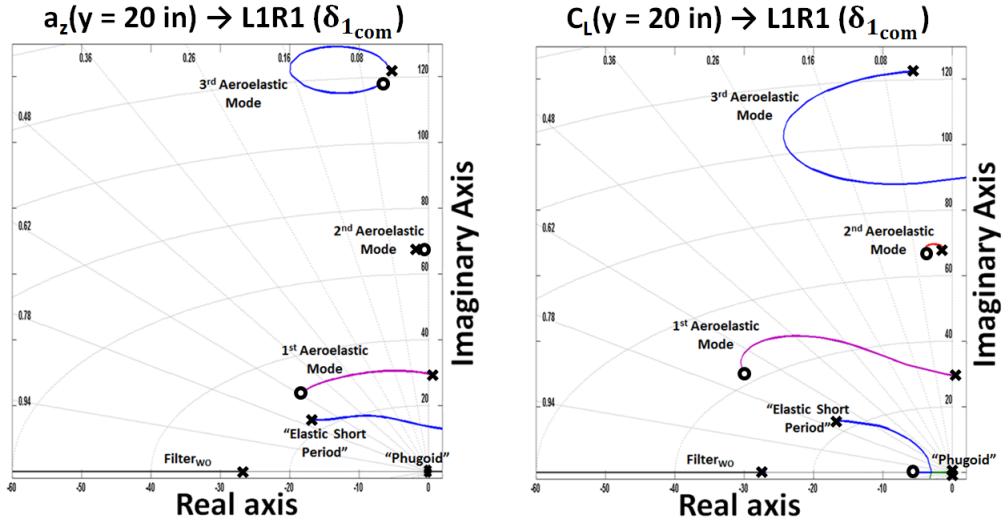


Figure 4.6: Root Locus Comparison of Controllers in Fig. 4.1 Including a Washout Filter

In Fig. 4.6, the filter is shown to change the behavior of the ESP mode (see Fig. 4.4 for comparison). Adding the filter tends to destabilize the ESP mode. The maximum amount of damping that can be achieved by both controllers including the washout filter is  $\zeta_{\text{BFF}} = 0.20$ . This damping value is also limited by  $\zeta_{\text{ESP}}$  of the  $a_z$ -Controller, this time reaching the lower bound in Eq. 4.1. At the same ESP damping ratio value, the  $C_L$ -Controller could reach a BFF mode damping of  $\zeta_{\text{BFF}} = 0.242$ , which is a 21% higher than the value of the  $a_z$ -Controller. The open-loop and the resulting closed-loop damping ratios of all the mode branches are included in Table 4.5. The  $a_z$ -Controller is again shown to result in a greater second aeroelastic mode damping. However, the total percentage damping of the second aeroelastic mode has decreased when compared to the controller that did not include the filter. The  $C_L$ -Controller is again shown to result in a greater damping of the third aeroelastic mode, which in this case it is greater than the total damping obtained by the controller that did not include the filter. Furthermore, the resulting losses in damping of the second aeroelastic mode by the  $C_L$ -Controller are less significant, which is a desired improvement. The classic robustness parameters gain and phase margins of both controllers are compared in Table 4.6.

Table 4.5: Comparison of Open-Loop and Closed-Loop Damping Ratios for Controllers in Fig. 4.1 Including a Washout Filter with  $\zeta_{\text{BFF}_{a_z}} = 0.6$  and  $\zeta_{\text{BFF}_{C_L}} = 0.64$

Controller	BFF Mode			2 <sup>nd</sup> Aeroelastic Mode			3 <sup>rd</sup> Aeroelastic Mode		
	Open-Loop $\zeta_{\text{BFF}}$	Closed-Loop $\zeta_{\text{BFF}}$	%-Increase	Open-Loop $\zeta_{\text{AE}_2}$	Closed-Loop $\zeta_{\text{AE}_2}$	%-Increase	Open-Loop $\zeta_{\text{AE}_3}$	Closed-Loop $\zeta_{\text{AE}_3}$	%-Increase
1 ( $a_z$ )	-0.0249	0.20	900	0.0204	0.0267	31	0.0466	0.0671	44
2 ( $C_L$ )					0.0189	-7		0.0902	94

Table 4.6: Comparison of Robustness Parameters for Controllers in Fig. 4.1 Including a Washout Filter with  $\zeta_{\text{BFF}} = 0.20$  (Both Controllers)

Controller	$K_p$ -Gain	Gain Margin (dB)		Phase Margin (deg.)		Gain-Crossover Frequency (rad/s)
1 ( $a_z$ )	0.00172	-16	4.3	-87	47	38
2 ( $C_L$ )	0.523	-21	32	-89	65	38

In Table 4.4, the  $C_L$ -Controller is again shown to have higher gain and phase margins than the  $a_z$ -Controller. The gain margins do not seem affected by the inclusion of the washout filter, which is to be expected since the filter dynamics lie in a range below the crossover frequency of both controllers. Nonetheless, the phase margins in Table 4.6 show more robust values, within the traditionally accepted range from 30 to 60 degrees. All in all, the  $C_L$ -Controller with the LESP sensor is still observed to be more suitable for suppressing the BFF mode. In addition, the bode diagram comparing the new *disturbance sensitivity* transfer functions is included in Fig. 4.7. Adding the washout filter is shown to not only increase the total damping of the BFF mode, but it is also shown to essentially maintain the lower-frequency dynamics unchanged.

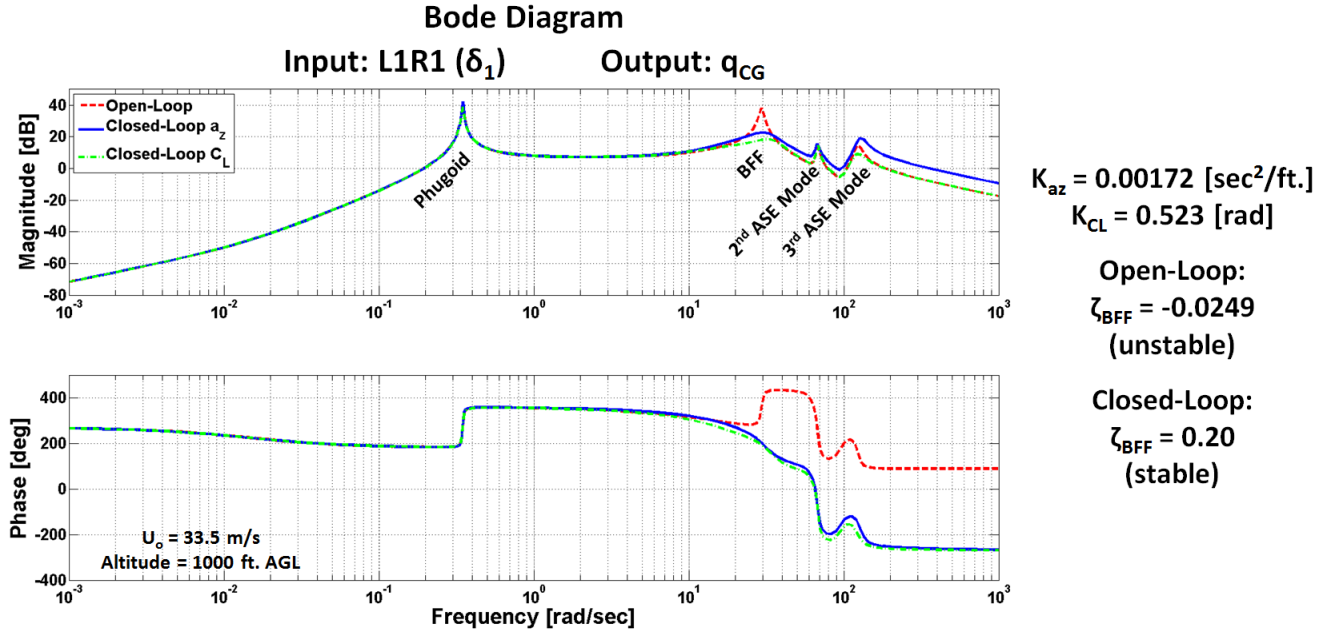


Figure 4.7: Bode Diagram of Disturbance Sensitivity Beyond Flutter Speed for Controller in Fig. 4.1 Including a Washout Filter

To assess the changes in attitude response of the augmented vehicle, the open-loop and closed-loop responses to a one-degree step input of the mid-board flap ( $\delta_3$ ) at both beyond the flutter speed (33.5 [m/s]) and below the flutter speed (26 [m/s]) are compared in Fig. 4.8. Note that, for a remotely-piloted aircraft, the pilot usually controls the aircraft based on the observed pitch attitude. Hence, it is important to keep the closed-loop pitch attitude response as unaffected as possible. Also, to maintain the same handling qualities, the aircraft's immediate response to pilot inputs must remain unaffected as well. Lastly, it is highly desirable to check that the aircraft's responses are not affected by the controller when the aircraft is flying below the flutter speed. In Fig. 4.8, both controllers are observed to have practically the same time response both beyond and below the flutter speed. When the aircraft is beyond the flutter speed, both controllers are observed to damp the unstable oscillations while keeping both the pitch attitude and the transient responses unaffected. Indeed, when the aircraft is below the flutter speed, the closed-loop responses of both controllers are observed to be practically identical to the open-loop response. Moreover, the control effort of both controllers to the step input in Fig. 4.8 are compared in Fig. 4.9. In Fig. 4.9, the  $C_L$ -Controller is shown to require a higher controller deflection than the  $a_z$ -Controller. Yet, the both controllers require a modest deflection of less than 1 degree. Also, the control effort after the system has been stabilized is shown to damp down to zero as oppose to tracking the sensed quantity. This effect is obtained thanks to the inclusion of the washout filter. Note that the phugoid mode of the augmented vehicle remains unstable using either controller. Yet, this unstable mode is of no concern as its frequency is so low that it can be easily stabilized by either the pilot's or autopilot's pitch-attitude control loop. In the next chapter, extra dynamics (e.g., actuator dynamics, sensor dynamics, and computational delays) are

added to the "perfect" system to check how the controllers behave in a model augmented to include parasite dynamics.

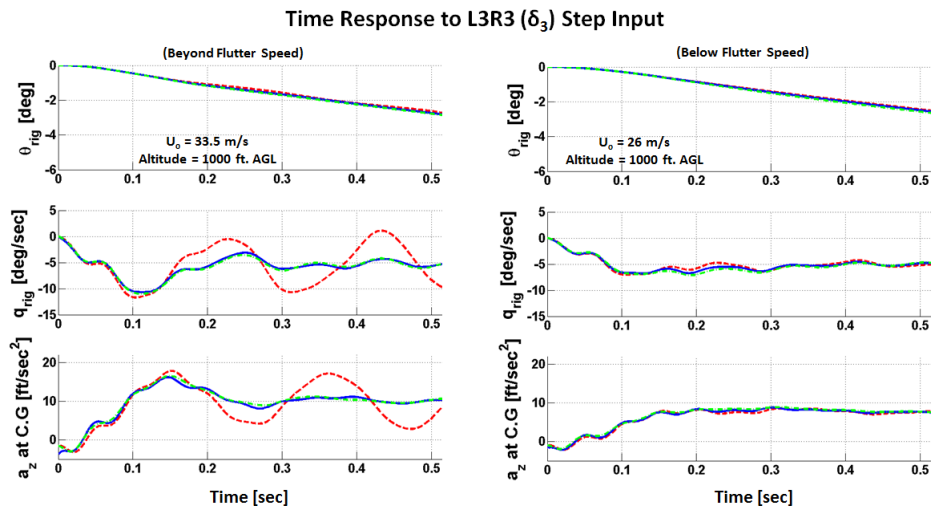


Figure 4.8: Time Response Comparison to a L3R3 ( $\delta_3$ ) Step Input

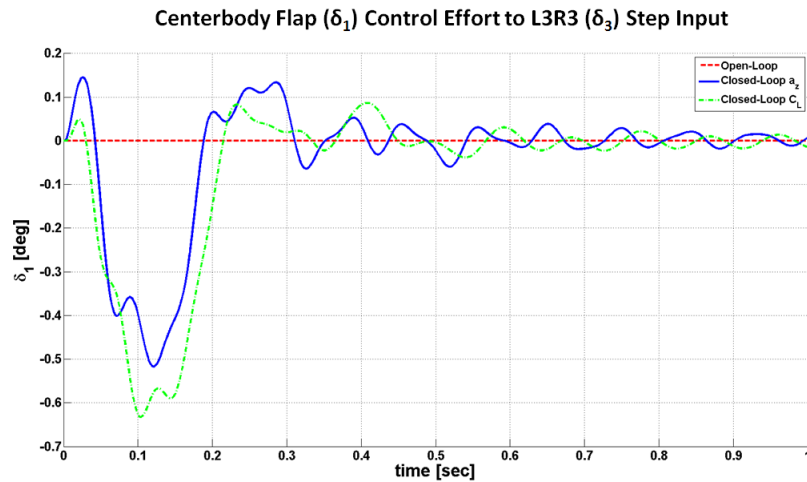


Figure 4.9: L1R1 ( $\delta_1$ ) Control Effort to the L3R3 ( $\delta_3$ ) Step Input in Fig. 4.8

# Chapter 5

## Robustness Analysis

In the previous chapter, the controllers were compared on their performance and robustness at stabilizing (and damping) the BFF mode of the mini-MUTT dynamic model with perfect sensors and actuators. In this chapter, the performance and robustness of both controllers are compared when including extra parasite dynamics that are present in most real systems. This chapter separates the study of parasite dynamics into three sections. Each section focuses on the study of one kind of parasite dynamic, which is augmented onto the previous model. The goal is to observe how sensitive the controllers are to each dynamic in order to gain a better understanding of the sources that may be most limiting to implementing the LESP sensor on a real system.

### 5.1 Actuator Dynamics

Up to this point, the actuator deflections were assumed to happen instantaneously. Obviously, this is not the case on a real system. Once the controller or flight computer sends a required deflection command, the servo-actuator starts deflecting continuously until it reaches such commanded deflection. These dynamics take an extra time, which can add a small lag to the system. Furthermore, real actuators have a finite bandwidth which may create a phase-loss and limited effect at higher frequencies. Consequently, the closed-loop block diagram in Fig. 4.1 is augmented to include the augmented actuator dynamics, as shown in Fig. 5.1.

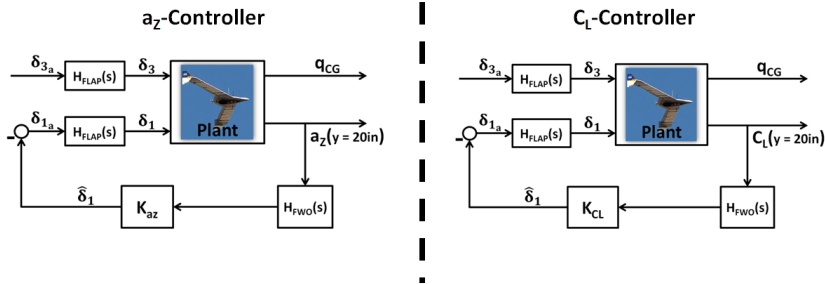


Figure 5.1: Block Diagram of Controllers Including Flap Actuator Dynamics

In Fig. 5.1,  $H_{FLAP}(s)$  represents the transfer function of the servo-actuator used to deflect the control flaps. The actuator used on the mini-MUTT is a Futaba S9254 servo. In [36], a second-order model of the servo-actuators is included to have the form in Eq. 5.1. This second order-model is obtained via frequency-domain system identification techniques and validated using the physical actuator.

$$H_{FLAP}(s) = \frac{96710}{s^2 + 840s + 96710} \quad (5.1)$$

Also, note the low-pass characteristics of the servo-actuator model in Eq. 5.1. At high frequencies, the transfer function in Eq. 5.1 is essentially zero, showing the loss of effectiveness. The root locus of the two updated controllers of this section are included in Fig. 5.2. The addition of the actuator dynamics causes a loss in effectiveness in damping the third aeroelastic mode. In fact, the  $a_z$ -Controller now tends to destabilize the third aeroelastic mode as opposed to stabilize it (see Fig. 4.6 for comparison). Another key observation is that the  $C_L$ -Controller could now destabilize the BFF mode for very large controller gains. Lastly, the second aeroelastic mode branch of the  $a_z$ -Controller is shown to have a small improvement when compared to the root locus in Fig. 4.6

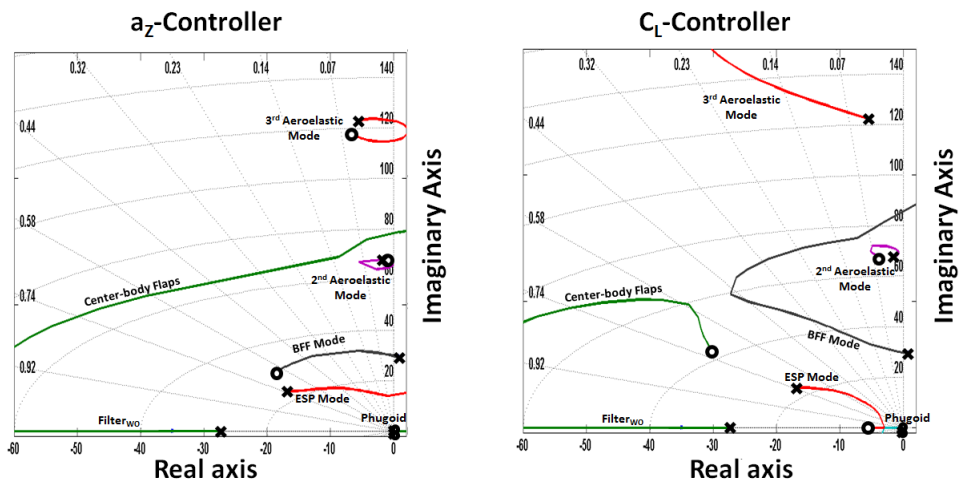


Figure 5.2: Root Locus Comparison of Controllers in Fig. 5.1

Following the same criteria than *Chapter 4*, the maximum amount of damping that can be achieved by both controllers in the current model is  $\zeta_{\text{BFF}} = 0.188$ . This maximum damping is also limited by the ESP mode of Controller reaching the lower bound in Eq. 4.1. At the same ESP damping ratio value, the  $C_L$ -Controller could achieve a maximum BFF mode damping of  $\zeta_{\text{BFF}} = 0.22$ . This damping ratio value would be 17% higher than the maximum damping ratio that can be achieved by the  $a_z$ -Controller. The performance of both controllers at damping the remaining modes is included in Table 5.1. The key observations to notice are how the damping of the third aeroelastic mode have been considerably reduced due to the limited bandwidth of the actuator at higher frequencies. The robustness characteristics of both controllers are included in Table 5.2. In Table 5.2, both controllers are shown to experience a loss of 10 degrees in PM as a consequence of including the actuator dynamics while the GMs and the gain-crossover frequencies remain more or less unchanged. Note that the gain margin of the  $a_z$ -Controller has actually increased. Yet, the phase-crossover frequency has decreased from virtually infinity to 121 [rad/s], which corresponds to the third aeroelastic mode branch.

Table 5.1: Comparison of Open-Loop and Closed-Loop Damping Ratios for Controllers in Fig. 5.1 with  $\zeta_{\text{BFF}_{a_z}} = 0.6$  and  $\zeta_{\text{BFF}_{C_L}} = 0.63$

Controller	BFF Mode			2 <sup>nd</sup> Aeroelastic Mode			3 <sup>rd</sup> Aeroelastic Mode		
	Open-Loop $\zeta_{\text{BFF}}$	Closed-Loop $\zeta_{\text{BFF}}$	%-Increase	Open-Loop $\zeta_{\text{AE}_2}$	Closed-Loop $\zeta_{\text{AE}_2}$	%-Increase	Open-Loop $\zeta_{\text{AE}_3}$	Closed-Loop $\zeta_{\text{AE}_3}$	%-Increase
1 ( $a_z$ )	-0.0249	0.188	855	0.0204	0.0289	42	0.0466	0.0225	-52
2 ( $C_L$ )	-0.0249	0.188	855	0.0204	0.0166	-19	0.0466	0.078	67

Table 5.2: Comparison of Robustness Parameters for Controllers in Fig. 5.1 with  $\zeta_{\text{BFF}} = 0.188$  (Both Controllers)

Controller	$K_p$ -Gain	Gain Margin (dB)	Phase Margin (deg.)	Gain-Crossover Frequency (rad/s)
1 ( $a_z$ )	0.00185	-15 : 5.3	-93 : 37	37
2 ( $C_L$ )	0.63	-20 : 28	-93 : 55	37

The bode diagram of the disturbance sensitivity for the system in Fig. 5.1 is depicted in Fig. 5.3. Although the comparison between the open-loop and the closed-loop frequency-response looks qualitatively very similar to the bode diagram in Fig. 4.7, notice the loss of phase at high frequencies. Similarly, the attitude responses to a mid-board flap step input beyond and below the flutter speed are depicted in Fig. 5.4. The attitude responses Fig. 5.4 resemble almost exactly the attitude responses in chapter 4. In the same way, the control

effort of the model including the actuator dynamics resemble almost exactly the response shown in the previous chapter (Fig. 4.9). For this reason, it was not included in this section. In the next section, the effects of including sensor dynamics are considered.

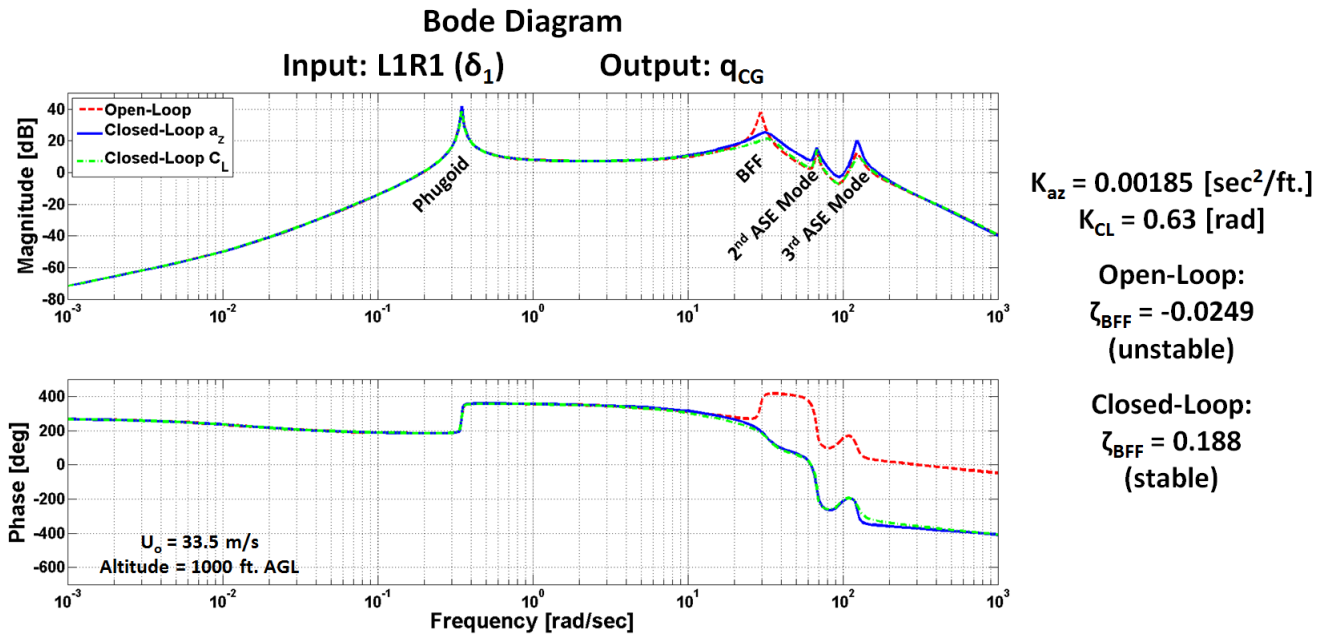


Figure 5.3: Bode Diagram of Disturbance Sensitivity Beyond Flutter Speed for Controllers in Fig. 5.1

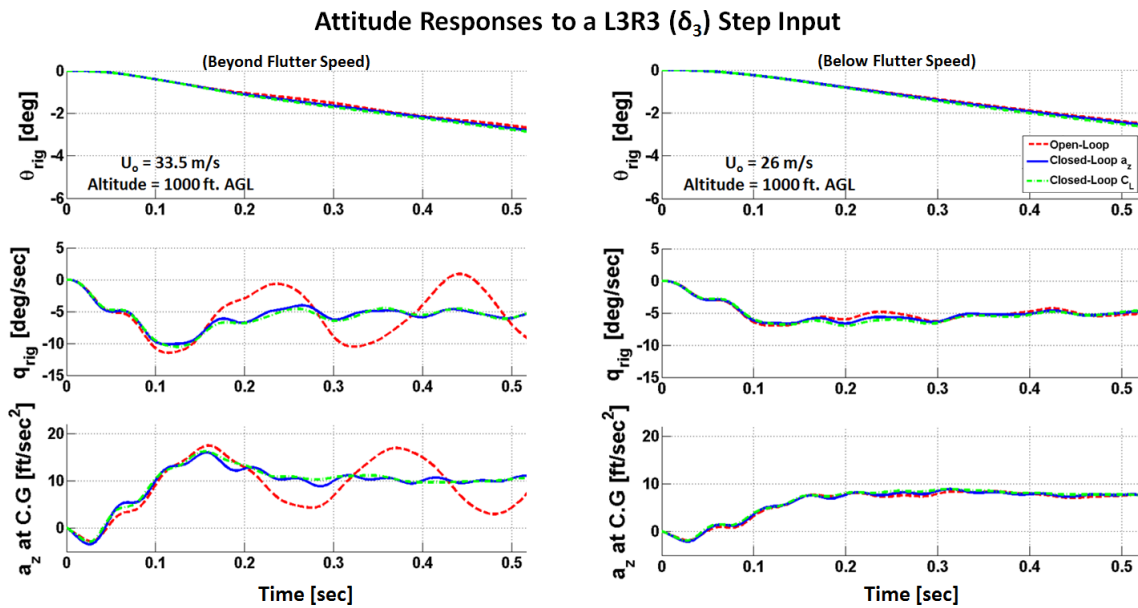


Figure 5.4: Time Response Comparison to a L3R3 ( $\delta_3$ ) Step Input for the System in Fig. 5.1

## 5.2 Sensor Dynamics

Analogous to the actuator dynamics, the same is true for the sensors. Many commercial sensors include low-pass filters in order to better reject high-frequency noise. Hence, the block diagram of both controllers are augmented to include the dynamics of the sensors, yielding the block diagrams depicted in Fig. 5.5. To simplify the comparison, note that both the accelerometer and the LESP sensor are assumed to have the same sensor dynamics. Adding the sensor dynamics is shown to have a low-pass effect.

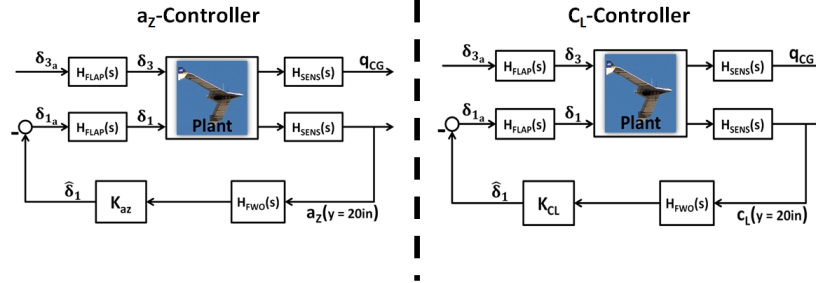


Figure 5.5: Block Diagram of Controllers Including Both Actuator and Sensor Dynamics

Here,  $H_{\text{SENS}}(s)$  represents the transfer function with the low-pass filter characteristics of the sensors. As the accelerometer in the mini-MUTT aircraft is filtered by a low-pass with a bandwidth of 35 Hz [36], the sensor transfer function is constructed as:

$$H_{\text{SENS}}(s) = \frac{2\pi 35}{s + 2\pi 35} \quad (5.2)$$

The root locus of the updated controllers of this section are included in Fig. 5.6. A key observation of the new controllers is the noticeable decrease in effectiveness on damping the BFF mode. Furthermore, the  $a_z$ -Controller can eventually make the BFF mode go unstable at higher controller gains. Now, the third aeroelastic mode branch of the  $a_z$ -Controller remains stable for all gains. Yet, the performance on damping the third aeroelastic mode has also been noticeably reduced. Lastly, the small improvement on the second aeroelastic mode damping that was noticed by the  $a_z$ -Controller on the previous section is observed to be lost again.

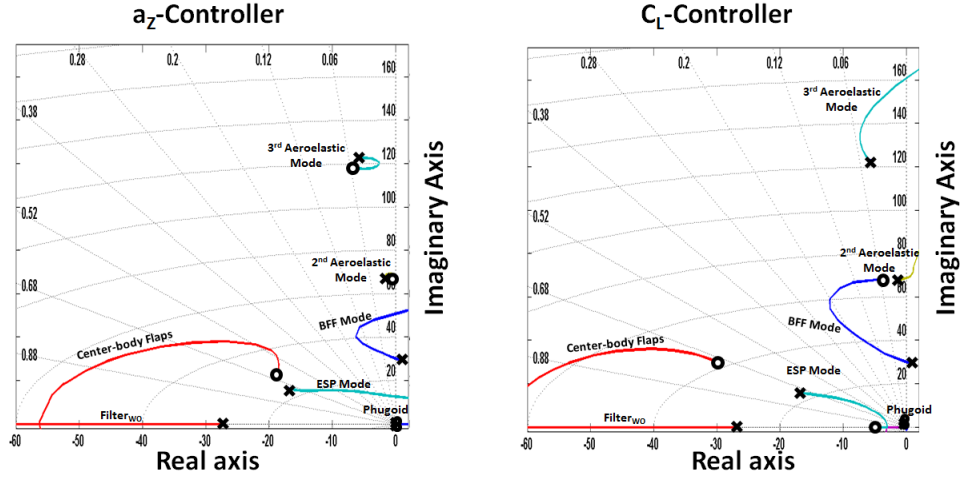


Figure 5.6: Root Locus Comparison of Controllers in Fig. 5.5

Following the same criteria than before, the maximum amount of damping on the BFF mode that can be achieved by both controllers is  $\zeta_{\text{BFF}} = 0.164$ , resulting on a 13% decrease from the design included on the previous section. Now, this damping value is limited by the short period mode of the  $a_z$ -Controller, which seems to be more sensitive to the augmented dynamics. At the same ESP damping ratio value, the  $C_L$ -Controller could reach a BFF mode damping of  $\zeta_{\text{BFF}} = 0.182$ . This damping ratio value would be an 11% higher than the maximum damping ratio that can be achieved by the  $a_z$ -Controller and only a 3% lower than the the damping ratio of the design on the previous section. The closed-loop performance of both controllers are included in Table. 5.3. As shown in Table 5.3, the percentage increase in most aeroelastic modes has decreased. The one exception is the percentage damping of the third aeroelastic mode by the  $a_z$ -Controller, which is less negatively affected. Yet, both controllers follow the same trend. The  $a_z$ -Controller achieves more damping on the second aeroelastic mode while achieving worse damping on the third aeroelastic mode, and the  $C_L$ -Controller does vice versa. The robustness parameters (GM and PM) of both controllers are included in Table 5.4.

Table 5.3: Comparison of Open-Loop and Closed-Loop Damping Ratios for Controllers in Fig. 5.5 with  $\zeta_{\text{BFF}_{a_z}} = 0.6$  and  $\zeta_{\text{BFF}_{C_L}} = 0.62$

Controller	BFF Mode			2 <sup>nd</sup> Aeroelastic Mode			3 <sup>rd</sup> Aeroelastic Mode		
	Open-Loop $\zeta_{\text{BFF}}$	Closed-Loop $\zeta_{\text{BFF}}$	%-Increase	Open-Loop $\zeta_{\text{AE}_2}$	Closed-Loop $\zeta_{\text{AE}_2}$	%-Increase	Open-Loop $\zeta_{\text{AE}_3}$	Closed-Loop $\zeta_{\text{AE}_3}$	%-Increase
1 ( $a_z$ )	-0.0249	0.164	760	0.0204	0.0248	22	0.0466	0.0297	-36
2 ( $C_L$ )	-0.0249	0.164	760	0.0204	0.0154	-24	0.0466	0.0559	20

Table 5.4: Comparison of Robustness Parameters for Controllers in Fig. 5.5 with  $\zeta_{\text{BFF}} = 0.164$  (Both Controllers)

Controller	$K_p$ -Gain	Gain Margin (dB)	Phase Margin (deg.)	Gain-Crossover Frequency (rad/s)
1 ( $a_z$ )	0.00183	-14 : 5.3	-100 : 28	36
2 ( $C_L$ )	0.668	-20 : <u>11</u>	-100 : <u>45</u>	38

Surprisingly, the GM of the  $a_z$ -Controller is shown to have increased slightly. However, it remains lower (less robust) than when compared to the  $C_L$ -Controller. Again, both controllers are shown to experience a loss of about 10 degrees in PM as a consequence of including the sensor dynamics. Up to this point, the phase seems to be a more limiting factor to damping the aeroelastic modes. The comparison between the open-loop and closed-loop attitude responses for both controllers are omitted in this section because all the responses do not seem to be greatly affected by the addition of the sensor dynamics. In other words, the attitude response plots seem almost identical to the plots in Fig. 5.4, so including them would be redundant.

### 5.3 Time Delays

Up to this point, the system was assumed to gather the data and produce a desired actuator command instantaneously. Yet, real systems have micro-controllers and processing computers that require a computational time. This computational time results in a small time delay introduced to the system. In this section, the processing time is modeled as a unique time delay added to the system as shown in Fig. 5.7.

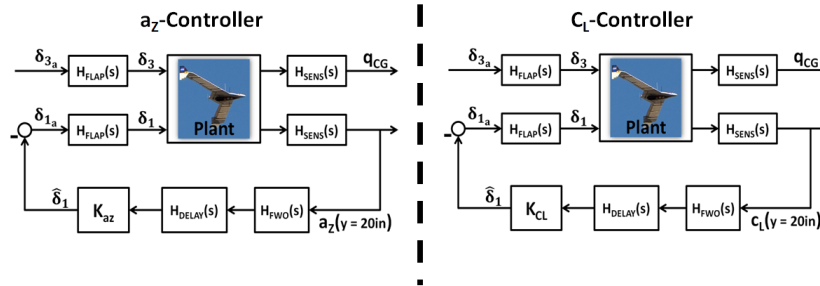


Figure 5.7: Block Diagram of Controllers Including Actuator Dynamics, Sensor Dynamics, and Time-Delay

In Fig. 5.7,  $H_{\text{DELAY}}(s)$  represents a transfer function that models the total delay. In

this case, the time-delay transfer function yields the following form:

$$H_{\text{DELAY}}(s) = e^{-\tau_{\text{ms}} s} \quad (5.3)$$

where  $\tau_{\text{ms}}$  is the value of the time delay in milliseconds. Now, the robustness of both controllers is directly affected by the addition of the time delay. Adding time delay causes a direct loss in phase that can eventually make the system go unstable. The relationship between time delay and the phase (in degrees) at a particular frequency of interest can be expressed as:

$$\text{Phase}(\omega) = \tau_{\text{ms}} \omega \frac{180}{\pi} \quad (5.4)$$

where  $\omega$  [rad/s] is the particular frequency of interest.

Using the expression in Eq. 5.4 and the design of the previous section (gains and robustness values as shown in Table 5.4), it is possible to solve for the maximum value of time delay that can be handled before each controller goes unstable. The main time-delay and phase results of both controllers are included in Table 5.5. The  $a_z$ -Controller can tolerate a maximum time delay of 13.6ms while the  $C_L$ -Controller can tolerate a maximum time delay of 21ms. In [36], the time required to run each component for a similar aircraft structure is included, adding up to a total time delay of 13.2ms. With such time delay, the  $a_z$ -Controller would be marginally stable with less than 1 degree of phase margin. On the other hand, the  $C_L$ -Controller would remain stable with 16 degrees of phase margin. Nonetheless, the author in [36] also includes a 1.5 safety factor to anticipate zero-order hold delays, resulting on a total time delay of 20ms. This time delay is beyond the maximum delay that the  $a_z$ -Controller can tolerate. On the other hand, the  $C_L$ -Controller would remain stable with 1.45 degrees of phase margin left. Yet, this phase margin may not be robust enough to tolerate extra uncertainty that is not included in the current model, making both controllers unsuitable for stabilizing the BFF mode with such gains.

Table 5.5: Time Delay and Corresponding Phase Results for Controllers in Fig. 5.7 with  $K_{a_z} = 0.00183$  and  $K_{C_L} = 0.668$

Controller	Available Phase Margin [deg.]	Maximum $\tau_{\text{ms}}$ [ms]	Phase Loss for $\tau_{\text{ms}} = 13.2$ ms [deg.]	Phase Margin Left [deg.]	Phase Loss for $\tau_{\text{ms}} = 20.0$ ms [deg.]	Phase Margin Left [deg.]	Phase Loss for $\tau_{\text{ms}} = 10.0$ ms [deg.]	Phase Margin Left [deg.]
1 ( $a_z$ )	28	13.6	27.2	0.8	41.3	-13.3	20.6	7.4
2 ( $C_L$ )	45	20.7	28.7	16.3	43.5	1.45	21.8	23.2
%-Increase	52	61						

Nonetheless, a root-locus study can be used to find the maximum damping ratio ( $\zeta_{\text{BFF}}$ ) that can be achieved by each controller, as well as the amount of time delay that would keep the BFF mode of each controller unstable for any proportional gain. The root-locus study

is conducted using the *Classical Control Design* toolbox in *MATLAB* using a second-order Padé approximation to account for the time delay of choice. The performance metrics of both controllers including the time delays of interest are included in Table 5.6. Note that a hypothetical time delay of 10ms is also included in the study in order to compare the performance of both controllers for a time-delay value that is further from the maximum limit of the  $a_z$ -Controller.

Table 5.6: Comparison of Open-Loop and Closed-Loop Damping Ratios for System in Fig. 5.7

		$\tau_{ms} = 20.0$ ms							
Controller	$K_p$ Gain	Open-Loop	Closed-Loop	Open-Loop	Closed-Loop	Open-Loop	Closed-Loop	GM [dB]	PM [deg.]
		$\zeta_{BFF}$	$\zeta_{BFF}$	$\zeta_{AE_2}$	$\zeta_{AE_2}$	$\zeta_{AE_3}$	$\zeta_{AE_3}$		
1 ( $a_z$ )	N.A.	-0.0249	N.A.	0.0204	N.A.	0.0466	N.A.	N.A.	N.A.
2 ( $C_L$ )	0.429	-0.0249	0.0125	0.0204	0.0188	0.0466	0.027	5.34	5
		$\tau_{ms} = 13.2$ ms							
1 ( $a_z$ )	0.00138	-0.0249	0.0152	0.0204	0.0188	0.0466	0.455	2.77	5
2 ( $C_L$ )	0.593	-0.0249	0.0585	0.0204	0.0170	0.0466	0.030	6.0	17
		$\tau_{ms} = 10.0$ ms							
1 ( $a_z$ )	0.00167	-0.0249	0.0406	0.0204	0.0191	0.0466	0.043	3.25	9
2 ( $C_L$ )	0.556	-0.0249	0.0802	0.0204	0.0185	0.0466	0.031	6.0	23

In Table 5.6, it is shown that the gain margin of the  $C_L$ -Controller can be moderately increased to 5 degrees by lowering the controller gain. Yet, the 20ms delay causes a major drop in performance as the BFF mode damping ratio goes from  $\zeta_{BFF} = 0.164$  to  $\zeta_{BFF} = 0.0125$ . All in all, the key observations of Table 5.6 are: (1) the performance of both controllers is shown to be greatly affected by the addition of time delays; (2) the  $C_L$ -Controller is shown to be more robust against time delays. Also, an example of the root-locus plots for  $\tau_{ms} = 13.2$  [ms] is depicted in Fig. 5.8. As argued using Table 5.6, Fig. 5.8 also shows that the  $C_L$ -Controller can achieve a greater damping of the BFF mode. Although it is not clearly shown in Fig. 5.8, the third aeroelastic mode branch becomes unstable at higher gains earlier than the second aeroelastic mode branch. Hence, the GM performance of the  $C_L$ -Controller is limited by the third aeroelastic mode. On the other hand, the BFF mode branch of the  $a_z$ -Controller is shown to become unstable at higher gains earlier than the ESP mode branch. Hence, the GM performance of the  $a_z$ -Controller is limited by the BFF mode. By observing root-locus plots similar to Fig. 5.8 at increasing  $\tau_{ms}$  values, it is possible to estimate the amount of time delay at which each controller will be unable to stabilize the BFF mode for any controller gain. The maximum amount of time delay that can be tolerated by the  $a_z$ -Controller is  $\tau_{ms} = 14$  [ms] while the  $C_L$ -Controller can handle up to  $\tau_{ms} = 20.4$  [ms].

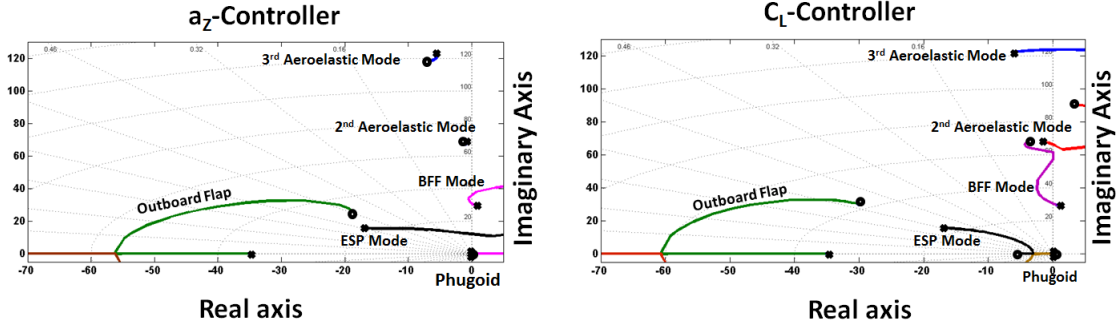


Figure 5.8: Root Locus Comparison of Controllers in Fig. 5.7 with  $\tau_{ms} = 13.2$  [ms]

Up to this point, the performance and robustness of the  $a_z$ -Controller and the  $C_L$ -Controller have been compared for designs including the washout filter and actuator dynamics, sensor dynamics, and time delays in a buildup manner. The robustness comparisons of all designs (Table 4.6, Table 5.2, and Table 5.4, and the new design including  $\tau_{ms} = 13.2$  [ms]) are summarized in Table 5.7. Again, it is important to emphasize that all data in Table 5.7 is obtained under the condition that both controllers have the same closed-loop values of  $\zeta_{BFF}$  and the closed-loop values of  $\zeta_{ESP}$  are within the range in Eq. 4.1. Note that the closed-loop values of  $\zeta_{ESP}$  may be different as long as both are within the accepted range. In Table 5.7, there are a few key observations: (1) the robustness metrics of the  $C_L$ -Controller all are higher than the robustness metrics of the  $a_z$ -Controller, for designs that achieve the same closed-loop value of  $\zeta_{BFF}$ ; (2) adding the parasite dynamics tends to negatively affect the GM of the  $C_L$ -Controller more than it affects the GM of the  $a_z$ -Controller; (3) the addition of actuator dynamics and sensor dynamics results in a common loss of about 10 degrees of PM (for each parasite dynamic) on both controllers; and (3) the parasite dynamic that is most limiting to the overall robustness of both controllers is the time-delay associated with the computational time of each step in the flight controller.

Also, it is important to recall that all designs were observed to be limited by the  $a_z$ -Controller reaching the  $\zeta_{ESP}$  boundary first. In other words, the  $C_L$ -Controller could attain a higher  $\zeta_{BFF}$  and still satisfy the condition in Eq. 4.1. In Table 5.8, the maximum values of closed-loop damping ratios that can be achieved by each controller and their corresponding robustness are included. Again, all the data in Table 5.8 is obtained under the condition that both controllers have the same closed-loop values of  $\zeta_{ESP}$ . In Table 5.8, the  $C_L$ -Controller is not only shown to offer greater  $\zeta_{BFF}$  values but it is also shown to offer more robust margins. On the other hand, the  $a_z$ -Controller is shown to offer designs that are less prone to worsen the damping ratio of the second aeroelastic mode. A symmetric deflection of the centerbody flaps is the control input that has the largest effect on the lift coefficient (i.e., has the largest  $C_{L_{\delta_1}}$ ) and the lowest effect on rigid-body dynamics (i.e., has the lowest  $C_{M_{\delta_1}}$ ). Hence, it would make sense that  $C_L$ -Controller, which can directly control the measured quantity, may have more advantages. On the other hand,  $a_z$ -Controller measures the structural acceleration and controls the lift coefficient which, in turn, causes a structural response. Hence, it may make sense that this controller has a bit of more lag, which is represented as a worse robustness.

Table 5.7: Robustness Parameters of All the Augmented Systems Designed to Have the Same Closed-Loop Value of  $\zeta_{BFF}$

	Controller	Gain Margin (dB)		Phase Margin (deg.)		Gain $K_p$	Gain-Crossover Frequency [rad/s]
		Value	%-Increase	Value	%-Increase		
System + Filter	1 ( $a_2$ )	4.3	644	47	38	0.00172	38
	2 ( $C_1$ )	<u>32</u>		<u>65</u>			
System + Filter + Flaps	1 ( $a_2$ )	5.3	428	37	49	0.00185	37
	2 ( $C_1$ )	<u>28</u>		<u>55</u>			
System + Filter + Flaps + Sensors	1 ( $a_2$ )	5.3	108	28	61	0.00183	36
	2 ( $C_1$ )	<u>11</u>		<u>45</u>			
System + Filter + Flaps + Sensors + 13.2 ms Delay	1 ( $a_2$ )	3	380	5	160	0.00138	35
	2 ( $C_1$ )	<u>14.5</u>		<u>13</u>			

Now, it is important to emphasize that the current flight-dynamics model does not account for unsteady aerodynamic effects. Yet, it was shown in [31] that the transfer function from the movement of the LESP position to the lift coefficient does not require lag states.

Table 5.8: Performance of All the Augmented Systems Designed to Have the Same Closed-Loop Value of  $\zeta_{ESP}$

	Controller	$\zeta_{BFF}$		$\zeta_{AE_2}$		$\zeta_{AE_3}$		GM [dB]		PM [deg.]	
		Value	%-Increase	Value	%-Increase	Value	%-Increase	Value	%-Increase	Value	%-Increase
1. System + Filter	1 ( $a_2$ )	0.2	21	<u>0.0267</u>	-30	0.0671	56	4.3	580	47	42
	2 ( $C_1$ )	<u>0.242</u>		<u>0.0188</u>		<u>0.105</u>		<u>29.23</u>		<u>67</u>	
2. System + Filter + Flaps	1 ( $a_2$ )	0.188	17	<u>0.0289</u>	-44	0.0225	318	5.87	353	37	48
	2 ( $C_1$ )	<u>0.22</u>		<u>0.0160</u>		<u>0.0940</u>		<u>26.6</u>		<u>55</u>	
3. System + Filter + Flaps + Sensors	1 ( $a_2$ )	0.164	11	<u>0.0248</u>	-40	0.0297	93	5.3	81	28	61
	2 ( $C_1$ )	<u>0.182</u>		<u>0.0150</u>		<u>0.0572</u>		<u>9.6</u>		<u>45</u>	
4. System + Filter + Flap + Sensor + 13.2 ms Delay	1 ( $a_2$ )	0.0152	285	<u>0.0190</u>	-11	<u>0.0455</u>	-34	2.77	104	5	240
	2 ( $C_1$ )	<u>0.0585</u>		<u>0.0170</u>		<u>0.030</u>		<u>5.66</u>		<u>17</u>	

# Chapter 6

## Conclusion

Flexible aircraft are a consequence of the aviation industry's pursuit to make air flight more efficient. The most challenging phenomenon of flexible aircraft is the presence of flutter. Hence, active flutter suppression is a key technology to avoid flutter across the entire flight envelope while still exploiting the performance benefits of flexible aircraft. The *Senflex*<sup>®</sup> hot-film sensor has shown it possible to measure the local lift coefficient in real time. This thesis compares the performance and the robustness of 2 similar controllers. One controller uses the lift coefficient output while the other uses the acceleration. Both controllers are designed to suppress the first aeroelastic (or BFF) mode of a flexible flying-wing UAV. The goal of this study is to study is to gain further understanding in the use of  $C_L$ -output for flutter suppression. Then, identify possible tradeoffs of future control systems that may integrate the *Senflex*<sup>®</sup> sensor. To ease the comparison, the control architecture of both controllers was chosen to be simple: a single-input and single-output proportional controller. The performance metric used for the comparison is the closed-loop damping ratio of the BFF mode. Yet, the closed-loop damping ratios of the remaining two aeroelastic modes were also observed for completeness. The robustness metrics used for the comparison were the classic gain and phase margins. First, both controllers are integrated onto a flight-dynamics model that includes only the "bare airframe". Later, this model is augmented to include actuator dynamics, sensor dynamics, and a computational time delay. The augmentation is done on a buildup manner to observe the effects that each parasite dynamic has on the total performance and robustness. All in all, the controller that used the  $C_L$ -output was shown to achieve greater damping on the BFF mode with greater robustness as well.

The key contributions of this thesis are: (1) a framework to include the local lift coefficient at anywhere across the wingspan as a system output; (2) the application of lift coefficient output for flutter suppression on a flight-dynamics model of a flexible drone; and (3) the performance and robustness comparison between lift coefficient output and acceleration output. By including the comparison, it may be easier for designers to consider the potential of the *Senflex*<sup>®</sup> sensor as the accelerometer sensor is well understood and has been widely used in many flutter suppression studies. The use of lift coefficient output for

flutter suppression has been recently studied. However, the present studies were integrated onto a pitch-and-plunge wing section and did not include the accelerometer comparison.

Future work includes considering the effects of modeling uncertainty that may be present in practice (e.g., mode shape uncertainty), testing the current findings on a wind-tunnel environment, and considering other control strategies. Examples of possible control strategies that could be considered include more "modern" control designs (e.g.,  $\mathcal{H}_\infty$ , LQR, etc) or a controller that integrates both accelerometer and lift coefficient measurements together. Again, it is important to emphasize that the current flight-dynamics model did not account for unsteady aerodynamics, which could have some effects on the flutter characteristics. Hence, future work would also include augmenting the flight-dynamics model to include unsteady aerodynamic effects.

# Bibliography

- [1] O. Bendiksen. Energy approach to flutter suppression and aeroelastic control. *Journal of Guidance, Control, and Dynamics*, 24(1), January 2001.
- [2] T. Bergman, A. Lavine, and F. Incropera. *Fundamentals of Heat and Mass Transfer, 7th Edition*. John Wiley & Sons, Incorporated, 2011.
- [3] M. Cook. *Flight Dynamics Principles: A Linear Systems Approach to Aircraft Stability and Control*. Elsevier aerospace engineering series. Elsevier Science, 2011.
- [4] R. Del Rosario, J. Koudelka, R. Wahls, and N. Madavan. Progress Towards Technologies in NASA’s Fixed Wing Project. *AIAA SciTech*, January 2014.
- [5] M. J. Dillsaver, C. E. Cesnik, and I. V. Kolmanovsky. Trajectory control of very flexible aircraft with gust disturbance. In *AIAA Atmospheric Flight Mechanics (AFM) Conference*, page 4745, 2013.
- [6] B. Etkin and L. Reid. *Dynamics of Flight: Stability and Control*. Wiley, 1995.
- [7] A. Gupta and P. Seiler. Ground vibration test on flexible flying-wing aircraft. *AIAA SciTech*, 2016.
- [8] H. Hesse, R. Palacios, and J. Murua. Consistent structural linearization in flexible aircraft dynamics with large rigid-body motion. *AIAA Journal*, 52(3):528–538, January 2014.
- [9] E. Houghton, P. Carpenter, S. Collicott, and D. Valentine. *Aerodynamics for Engineering Students*. Elsevier Science, 2012.
- [10] A. Kharina and D. Rutherford. Fuel efficiency trends for new commercial jet aircraft: 1960 to 2014. published as white paper in *ICCT*, September 2015.
- [11] A. Kotikalpudi, H. Pfifer, and G. J. Balas. Unsteady aerodynamics modeling for a flexible unmanned air vehicle. *AIAA Atmospheric Flight Mechanics Conference*, 2015.
- [12] T. Kuphaldt. *Lessons in Electric Circuits. Vol. 1-DC*. Design Science License, 2006.
- [13] E. Livne. The active flutter suppression (AFS) technology evaluation project. Presented at the 2014 Technical Review Meeting of the FAA Joint Advanced Materials and Structures (JAMS). Center of Excellence, Seattle, WA, March 2014.

- [14] J. Mahesh, C. Stone, W. Garrard, and H. Dunns. Control law synthesis for flutter suppression using linear quadratic gaussian theory. *Journal of Guidance, Control, and Dynamics*, 4(4):415–422, 1981.
- [15] A. Mangalam and M. Brenner. Fly-by-feel sensing and control: Aeroservoelasticity. *AIAA Atmosphere Flight Mechanics Conference*, June 2014.
- [16] A. Mangalam and T. Moes. Real-time unsteady loads measurements using hot-film sensors. 22<sup>nd</sup> *AIAA Applied Aerodynamics Conference*, August 2004.
- [17] S. Mangalam. Method and system for locating critical flow feature indicators in three dimensional flow regimes, June 14 2006. EP Patent App. EP20,040,788,552.
- [18] L. Meirovitch and I. Tuzcu. Time simulations of the response of maneuvering flexible aircraft. *Journal of Guidance, Control, and Dynamics*, 27(5):814–828, September 2004.
- [19] E. Morelli. Real-time aerodynamic parameter estimation without air flow angle measurements. *Journal of Aircraft*, 49(4), 2012.
- [20] H. Pfifer and B. Danowsky. System identification of a small flexible aircraft. *AIAA SciTech*, 2016.
- [21] A. E. Pontzer, M. D. Lower, and J. R. Miller. Unique aspects of flight testing unmanned aircraft systems. Technical report, DTIC Document, 2010.
- [22] A. Preumont. *Vibration control of active structures: an introduction*, volume 179. Springer Science & Business Media, 2011.
- [23] J. Ryan and J. Bosworth. Current and future research in active control of lightweight, flexible structures using the x-56 aircraft. *AIAA SciTech*, 2014.
- [24] D. Schmidt. *Modern Flight Dynamics*. McGraw-Hill Education, 2011.
- [25] D. Schmidt. Stability augmentation and active flutter suppression of a flexible flying-wing drone. *Submitted to Journal of Guidance, Control, and Dynamics*, 2015.
- [26] D. Schmidt, W. Zhao, and R. Kapania. Flight-dynamics and flutter modeling and analysis of a flexible flying-wing drone. *AIAA Atmospheric Flight Mechanics Conference*, January 2016.
- [27] P. Sforza. *Commercial Airplane Design Principles*. Elsevier aerospace engineering series. Elsevier Science, 2014.
- [28] F. Silvestre and P. Paglione. Dynamics and control of a flexible aircraft. *AIAA Atmospheric Flight Mechanics Conference and Exhibit*, August 2008.
- [29] B. Stevens, F. Lewis, and E. Johnson. *Aircraft Control and Simulation: Dynamics, Controls Design, and Autonomous Systems*. Wiley, 2015.

- [30] V. Suryakumar, Y. Babbar, T. Strganac, and A. Mangalam. Control of a nonlinear wing section using fly-by-feel sensing. *AIAA Atmosphere Flight Mechanics Conference*, June 2015.
- [31] V. Suryakumar, Y. Babbar, T. Strganac, and A. Mangalam. An unsteady aerodynamic model based on the leading-edge stagnation point. *AIAA Applied Aerodynamics Conference*, June 2015.
- [32] V. S. Suryakumar, Y. Babbar, T. W. Strganac, and A. S. Mangalam. Control of a nonlinear wing section using fly-by-feel sensing. In *AIAA Atmospheric Flight Mechanics Conference*, page 2239, 2015.
- [33] V. S. Suryakumar, A. S. Mangalam, Y. Babbar, and T. W. Strganac. A load-based feedback approach for distributed aeroservoelastic control. In *AIAA Atmospheric Flight Mechanics Conference*, page 3101, 2016.
- [34] T. Systems. Constant voltage anemometer - technical note.
- [35] A. Tewari. *Aeroservoelasticity: Modeling and Control*. Control Engineering. Springer New York, 2015.
- [36] J. Theis, P. Harald, and P. Seiler. Robust control design for active flutter suppression. *AIAA Atmospheric Flight Mechanics Conference*, 2016.
- [37] T. Theodorsen. General theory of aerodynamic instability and the mechanism of flutter. Tech. Rep. NACA-496, *National Advisory Committee for Aeronautics*, 1935.
- [38] M. Waszak and D. Schmidt. Flight dynamics of aeroelastic vehicles. *Journal of Aircraft*, 25(6):563–571, 1988.
- [39] M. R. Waszak and S. Srinathkumar. Flutter suppression for the active flexible wing-a classical design. *Journal of Aircraft*, 32(1):61–67, 1995.
- [40] T. Weisshaar. Aircraft aeroelastic design and analysis. Published at Purdue University’s website as class notes, July 2009.
- [41] R. Williams and D. Lawrence. *Linear State-Space Control Systems*. John Wiley & Sons, 2007.
- [42] L. Woods. *The Theory of Subsonic Plane Flow*. Cambridge aeronautical series. Cambridge University Press, 2011.
- [43] J. Wright and J. Cooper. *Introduction to Aircraft Aeroelasticity and Loads*. Aerospace Series. Wiley, 2014.
- [44] J. Wykes, C. Borland, M. Klepl, and C. MacMiller. Design and development of a structural mode control system. *NASA/CR*, 143846, 1977.

- [45] J. H. Wykes, T. R. Byar, C. J. Macmiller, and D. C. Greek. Analyses and tests of the b-1 aircraft structural mode control system. 1980.
- [46] G. Xiong and C. Yang. Synthesis on flutter suppression control law for active aeroelastic wing. *AIAA Paper*, 1463:2001, 2001.
- [47] E. C. Yates Jr. Calculation of flutter characteristics for finite-span swept or unswept wings at subsonic and supersonic speeds by a modified strip analysis. 1958.
- [48] J. Zeng, J. Wang, R. de Callafon, and M. Brenner. Suppression of the aeroelastic/aeroservoelastic interaction using adaptive feedback control instead of notching filters. In *AIAA Atmospheric Flight Mechanics Conference*, page 6459, 2011.